Journal of Structural Geology 31 (2009) 11–28

Contents lists available at ScienceDirect

Journal of Structural Geology

journal homepage: www.elsevier.com/locate/jsg

Tectonic evolution of the Ganos segment of the North Anatolian Fault (NW Turkey)

C. Janssen [a,*], M. Bohnhoff [a], Y. Vapnik [b], E. Görgün [a], F. Bulut [a], B. Plessen [a], D. Pohl [a], M. Aktar [c], A.I. Okay [d], G. Dresen [a]

[a] GeoForschungsZentrum, Telegrafenberg, D-14473 Potsdam, Germany
[b] Department of Geological and Environmental Sciences, Ben Gurion University of the Negev, Beer-Sheva 84105, Israel
[c] Bogazici University, Kandilli Observatory and Earthquake Research Institute, Cengelköy, 81220 Istanbul, Turkey
[d] Istanbul Technical University, Eurasia Institute of Earth Sciences and Faculty of mines, Department of Geology, Maslak 34680 Istanbul, Turkey

ARTICLE INFO

Article history:
Received 25 February 2008
Received in revised form
12 September 2008
Accepted 30 September 2008
Available online 1 November 2008

Keywords:
Ganos fault
Seismicity
Fault architecture
Fluid inclusions
Stable isotopes
Turkey

ABSTRACT

We analyzed the paleostress field, ongoing deformation, meso- to micro-scale faulting, cataclasis, fault rock alteration and veining within turbidite and limestone sequences at the Ganos Fault which represent a major branch of the North Anatolian Fault Zone in NW Turkey. Fault damage was found to occur across a several kilometers wide zone. Effects of faulting are shown by localized subsidiary brittle faults and fault rock alteration in the turbidites as well as fault breccia formation in the limestone sequence. Microseismicity along the Ganos Fault cluster at two locations, the more pronounced being located offshore at a fault bend associated with a change from a transpressional to a transtensional regime. Kinematic analysis reveals a dextral strike-slip regime with components of normal and thrust faulting. Along strike paleostress orientation at the Ganos Fault is rather uniform. Deformation mechanisms and fluid inclusion data from quartz and calcite veins suggest that fault-related quartz veins were formed at temperatures between 170 and 250 °C and pressures between 40 and 120 MPa. Fault-related calcite vein growth occurred during a temperature decrease from 170 °C to 70 °C with pressures likely below 50 MPa. Fluid inclusion and stable isotope data show that the fluids are predominantly of meteoric origin and migrated upwards into the fault. Pure CH_4 inclusions in quartz also suggest a biogenic or thermogenic methane origin.

1. Introduction

The North Anatolian Fault Zone (NAFZ) is the most active plate-bounding strike-slip fault in Europe and has developed in the framework of the northward moving Arabian plate and the Hellenic subduction zone where African lithosphere is subducting below the Aegean (e.g. Sengör, 1979). Extending along 1600 km between Eastern Anatolia and the North Aegean, it predominantly forms a right-lateral strike-slip plate boundary that slips at an average rate of 10–24 mm/yr (e.g. Barka, 1992; Reilinger et al., 2006). During the last century, the NAFZ has ruptured over 900 km of its length in a series of large events starting in 1939 near Erzincan in Eastern Anatolia and propagating toward the West (Ambraseys, 1970; Barka, 1992). The last events in the broader Marmara region were the 1912 Mw = 7.3 event on the Ganos Fault (e.g. Ambraseys, 2001; Altunel et al., 2004) at the western end and the Izmit Mw = 7.4 and Düzce Mw = 7.1 events of 1999 (e.g. Tibi et al., 2001; Barka et al., 2002) at the eastern end. The Sea of Marmara represents a more than 100 km long seismic gap that did not rupture since 1766 and that is believed being capable of generating two $M \geq 7.4$ earthquakes within the next decades (e.g. Hubert-Ferrari et al., 2000).

Seismogenic faulting occurs within the upper 5–20 km of the crust and is therefore not accessible to direct observations. As a result, geological field investigations of faults exhumed from seismogenic depth, geochemical analyses of fault rocks and geophysical studies have been used to constrain the evolution of fault zones and to test fault zone models (e.g. Chester and Logan, 1986; Schulz and Evans, 2000; Janssen et al., 1998, 2004).

In this paper we examine the fault-related deformation of the Ganos Fault (GF), as one major branch of the NAFZ in NW Turkey (Fig. 1a). Despite the important role of the GF for seismic activity, tectonics and morphology of the Ganos-Saros region (e.g. Hancock and Erkal, 1990; Tüysüz et al., 1998; Okay et al., 1999; Yaltirak, 2002; Yaltirak and Alpar, 2002; Okay et al., 2004; Altunel et al., 2004; Seeber et al., 2004; Zattin et al., 2005) the knowledge of fault structures, fault evolution (including fault kinematics and

* Corresponding author. Tel.: +49 331 2881323; fax: +49 331 2881328.
E-mail address: jans@gfz-potsdam.de (C. Janssen).

0191-8141/$ – see front matter © 2008 Elsevier Ltd. All rights reserved.
doi:10.1016/j.jsg.2008.09.010

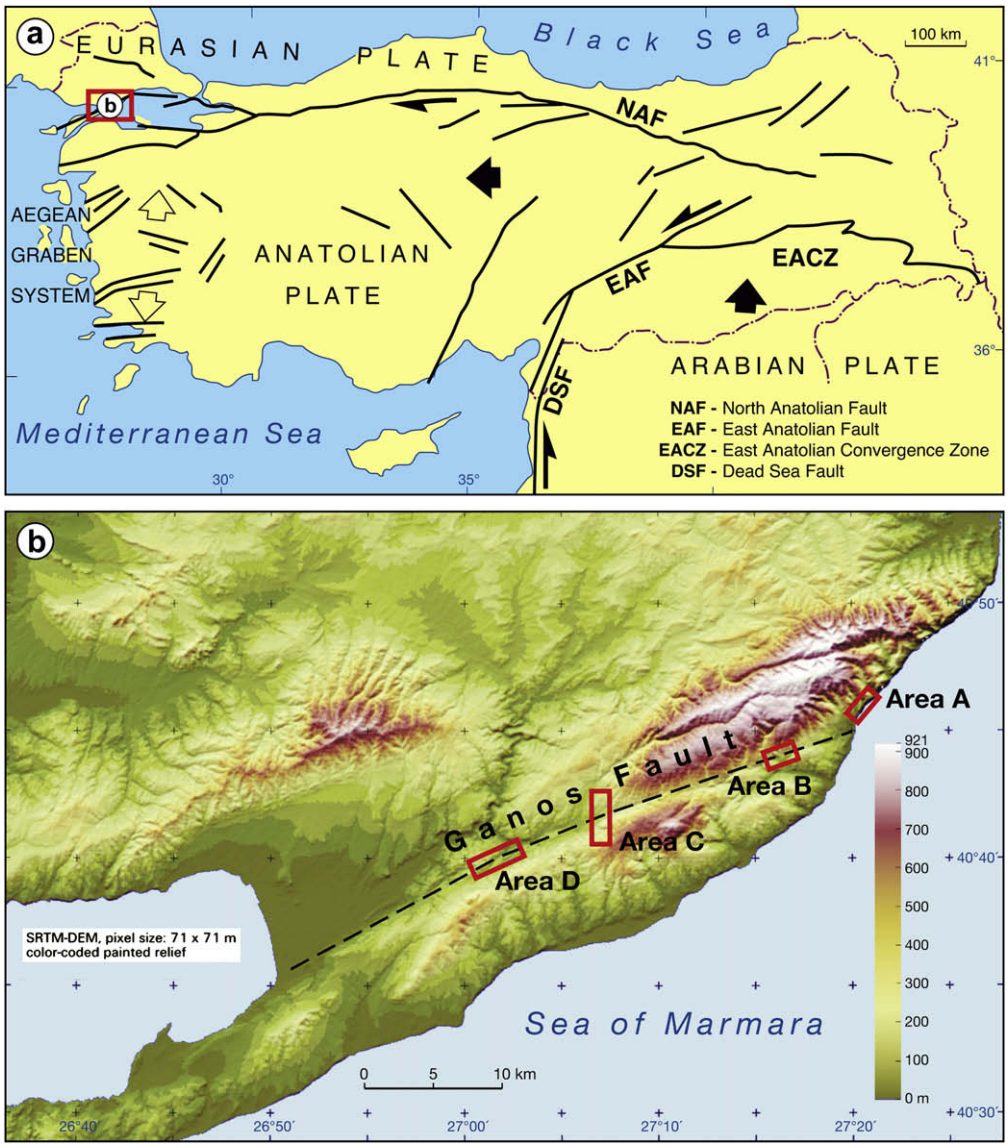

Fig. 1. Regional setting of the North Anatolian Fault Zone. (a) Geotectonic map of the Anatolian block, showing the relative movements of the Arabian plate, and the Anatolian block (filled arrows), and the N–S extension in the Aegean graben system (outlined arrows). (b) Satellite image of the Ganos Fault with areas of detailed investigations.

deformation conditions), seismicity, and fault–fluid relations is rather incomplete. In this study we address these issues examining the structure and seismicity of the GF using structural and geochemical investigations and low-detection threshold seismic monitoring.

Spatial distribution of the microseismicity provides information about active faulting and focal mechanisms allow to determine the local faulting regimes. The evaluation of meso- and microscopic structures of the exhumed fault portions provides direct information about the fault structure and composition of fault rocks and the evolution of the fault zone. Fluid inclusion analyses from quartz and calcite veins are used to examine faulting deformation conditions. Stable isotope data help to relate fluid involvement to faulting processes. Four locations close to the fault trace were examined in detail (Fig. 1b).

2. Geological setting of the Ganos Fault zone

The GF forms a 45 km long linear fault system and represents the link between the northern strand of the NAFZ in the Sea of Marmara and the North Aegean Trough where slip partitioning results in branching of the fault zone (e.g. Barka and Kadinsky-Cade, 1988; Okay et al., 1999). The GF consists of several sub-parallel faults, which are separated by less than 1 km (Okay et al., 2004). The trace of the fault is clearly discernable on satellite images with its northeastern part being bounded by the Ganos mountains (Fig. 1b). A dominant right-lateral strike-slip motion became active toward the end of the Miocene and formed the Ganos Mountains due to transpressional uplift (Tüysüz et al., 1998; Okay et al., 1999). Since the latest Miocene the total accumulated right-lateral displacement is in the order of 40 km (Okay et al., 1999). Armijo et al. (1999) has published a cumulative offset of 85 km. However, their criteria were challenged by Yaltirak et al. (2000, see also Sengör et al. 2005). At present, the GF accommodates fault-normal convergence at a rate of 1.1 ± 0.4 mm/yr (Okay et al., 2004). Tüysüz et al. (1998) interpreted the apparent lack of seismicity for magnitudes larger than 3 along the GF as an indication for a locked fault segment that slips only during large earthquakes. Recent interferometry and GPS measurements estimated a fault locking depth in the range of ~8–17 km (Motagh et al., 2007).

The internal structure of the exhumed parts of the GF reveals a structural complexity with predominant transpressive structures along the main strand of the GF and transtensional features in the transition area from the Ganos Mountains to the Tekirdag Basin (Okay et al., 1999; Seeber et al., 2004).

3. Seismicity at the Ganos Fault

Seismicity in the western Marmara Sea region predominantly occurs offshore along the main branch of the NAFZ (Boğaziçi University Kandilli Observatory and Earthquake Research Institute/KOERI, earthquake catalogue for 1900–2005; Fig. 2). The KOERI catalogue for the GF region is complete down to a magnitude of $M_c = 2.7$. Interestingly, the GF is almost aseismic down to this magnitude threshold and a diffuse distribution of hypocenters is observed offshore. In particular, seismicity clusters occur NW of Marmara Island and in the Tekirdağ Basin. The three largest earthquakes in the GF region during the last century occurred in 1912 within only a few days. Two events occurred along the GF with surface wave magnitudes (M_s) of 7.3 (see red star in Fig. 2) and $M_s = 6.2$, respectively. The rupture of the 1912 mainshock extended along the entire onshore segment between Marmara Sea and Gulf of Saros. Based on seafloor observations, Armijo et al. (2005) suggested that the rupture even extended into the Marmara Sea. The last earthquake at the GF ($M > 4$) occurred in 1985 in the Ganos mountains with a reverse faulting mechanism on a NE striking fault plane (Kalafat, 1995).

In order to observe the microseismic activity at the GF at low magnitude-detection threshold, a local temporary network was operated at the eastern part of the fault for a period of 70 days. Spatiotemporal behavior of microseismic activity was analyzed using conventional location techniques and statistical methods focusing on the role of the GF for the seismotectonic setting of this region.

3.1. Database

A total of eight seismic stations were deployed that covered the eastern portion of the GF (see Fig. 3a). In addition we also used recordings from the 4 permanent National Earthquake Monitoring Center (NEMC) seismic stations in the region. The network was in operation between 27th Sep. and 5th Dec. 2005. Fig. 3a (left) shows the station distribution where red and black triangles represent temporary and permanent stations, respectively. The average station spacing is ~2 km. Temporary stations were equipped with short-period seismometers of Type MARK L4-3D (eigenfrequency 1 Hz) and portable field recorders of type EDL. Power supply was realized using rechargeable batteries and solar panels. NEMC stations were permanently equipped with CMG-40 T and CMG-3ESPD Güralp broadband sensors.

Data were continuously recorded at 100 samples per second on three components. To evaluate the data, we ran a STA/LTA (short-term average/long-term average) trigger on the vertical component of each station as a first step. In general, events were selected if passing a coincidence trigger (>4 stations) combined with an algorithm neglecting events far outside the network. Phase onsets were picked manually. Absolute hypocenter determination was performed using the HYPOCENTER earthquake location program (Lienert and Havskov, 1995) based on P-wave and S-wave arrivals. An initial 1-D velocity model proposed by Karabulut et al. (2002) was used to locate the events. We iteratively varied the initial hypocentral depths between 1 and 25 km and proceeded with the solution resulting in the lowest errors.

3.2. Results

A total of 115 events were observed and located during the 70 days recording period. The distribution of hypocenters is plotted in Fig. 3a and b in map view and as depth section, respectively. Two seismically active regions were identified, one along the GF itself and the second offshore NW of Marmara Island. All events occurred within the uppermost 16 km depth (Fig. 3b, right). For comparison we also displayed the KOERI catalogue locations for the same time interval in Fig. 3a (left) exhibiting only 11 events. The depth distribution of events located by NEMC is between 5 and 20 km except one outlier (Fig. 3b, left).

Local magnitudes (M_l) were calculated following the procedure given by Baumbach et al. (2003) and Bindi et al. (2007) based on an updated attenuation curve and revised station corrections for the temporary stations. The procedure involves automatic estimation of M_l for all events at each station deconvolving the traces to synthetic Wood-Anderson torsion seismograms using instrument response and maximum horizontal peak amplitudes. Fig. 3c (right) shows the magnitude-frequency distribution for the obtained seismicity catalogue. The overall magnitude threshold of completeness (M_c) is 0.6 and the largest event had a magnitude of 2.5. For reference we also plotted the KOERI catalogue for the same time interval in Fig. 3c (left). The significant difference between

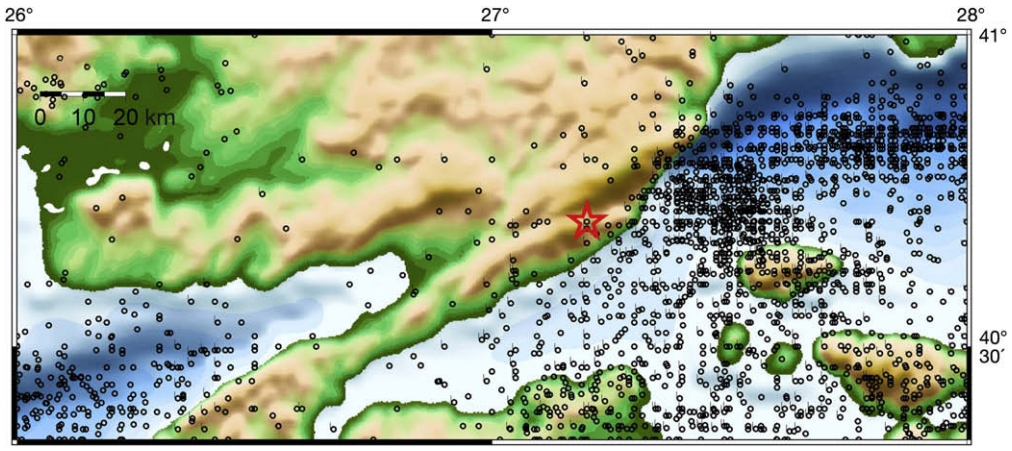

Fig. 2. Seismic activity at the Ganos Fault region between 1900 and 2005. The data were taken from the KOERI catalogue (http://www.koeri.boun.edu.tr/sismo/veri_bank/mainw.htm) that is complete for $M > 2.7$. The open red star represents the 9 August 1912 ($M_s = 7.3$) Mürefte-Şarköy earthquake (Ambraseys, 2001). Most events of the KOERI catalogue are located offshore below the Sea of Marmara and only few events are associated with the Ganos Fault itself. (For interpretation of the references to colour in this figure legend, the reader is referred to the web version of this article).

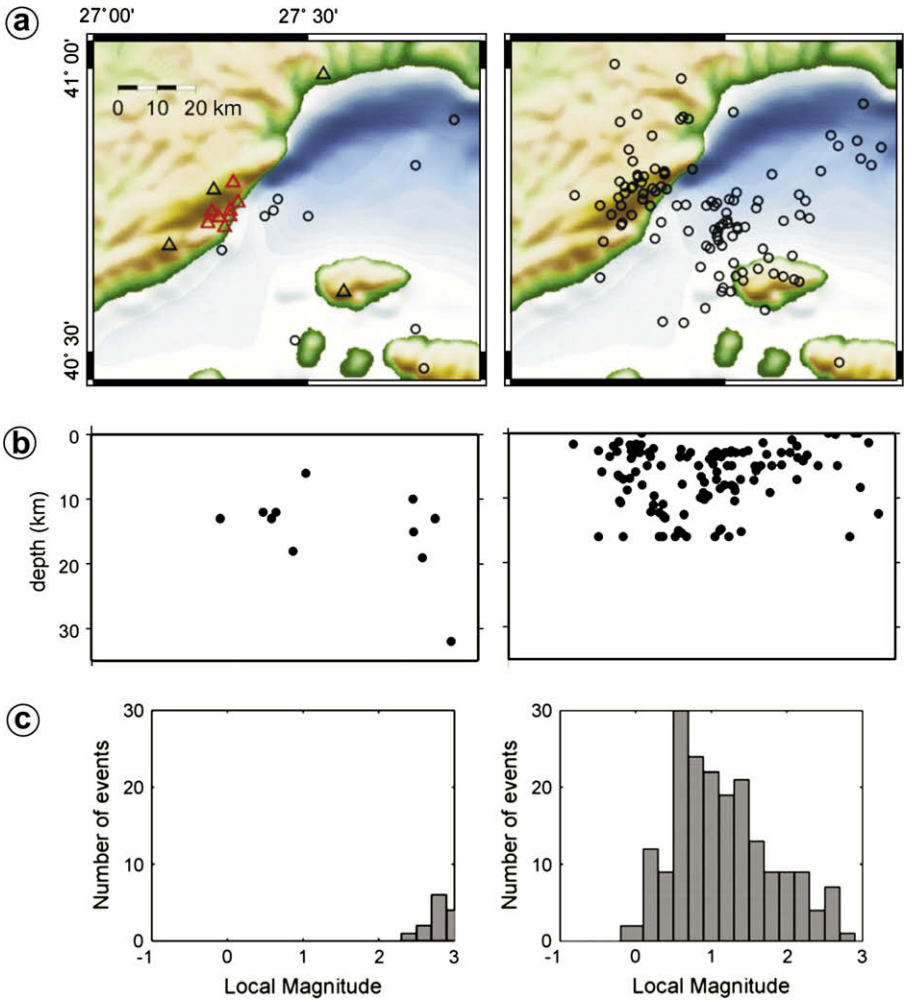

Fig. 3. (a) Distribution of the permanent and temporary seismic stations along the Ganos Fault. The red open triangles represent temporary stations and the black triangles represent permanent NEMC stations (left). Black open circles mark earthquakes observed during deployment of the temporary network. A substantial portion of the observed seismicity is located offshore NW of Marmara Island and along the Ganos Fault (right) (b) Depth distribution of hypocenters recorded exclusively by the permanent NEMC stations (left) and by the entire network (right). (c) Magnitude-frequency relationship for both catalogs. The magnitude of completeness was significantly reduced from 2.5 (permanent stations) to 0.6 (permanent and temporary stations). (For interpretation of the references to colour in this figure legend, the reader is referred to the web version of this article).

both catalogs exemplifies the advantage of densely spaced temporary seismic networks to evaluate small-scale brittle deformation in selected areas.

Microearthquakes in this experiment are too small ($M_l < 2$) to determine reliable focal mechanisms for individual events. Instead, we determined a cumulative fault plane solution for each cluster based on P-wave polarities using a grid search algorithm (FOCMEC, Snoke, 2003). Pressure (P) and Tension (T) quadrants are indicated by white and red colours, respectively (Fig. 9c).[1] Plus (+) and mines (−) are station distributions in the focal sphere. This cumulative focal mechanism reveals a strike-slip regime with a minor dip-slip (55°) component (Fig. 9c, lower hemisphere projection).

4. Meso-structural patterns of faulting

4.1. Methods

Subsidiary faults with associated striations observed in the field along the GF were used to estimate local incremental strain tensors with shortening and extension axes (program FaultKin 4.0, Allmendinger, 2001; Maret and Allmendinger, 1990). In a second step, a stress-tensor inversion was applied to the data in order to determine the orientation of the three principal stress axes (σ_1 = maximum, σ_2 = intermediate and σ_3 = minimum) as well as the relative stress magnitude R $(\sigma_1 - \sigma_2)/(\sigma_1 - \sigma_3)$, $0 < R < 1$ (Michael, 1991; see also Bohnhoff et al., 2004, 2006) for time covered by the input data. Data were collected in all four sub-areas of the GF (Fig. 1b). However, a sufficient number of fault-slip data was found only in sub-areas A, C and D.

The amount of brittle fault-related deformation (damage density) was quantified using the line intersection method from Hudson and Priest (1983), which is based on counting the intersections of subsidiary faults, fractures and veins per meter.

4.2. Fault rocks, subsidiary faults and veins at outcrop scale

Study-area (*profile*) *A* is located northeast of the village Gaziköy, were the GF enters the Marmara Sea (Fig. 4a). Here the fault separates turbidites (siltstone and shale) of the Gaziköy Formation (mid-Eocene) from Miocene sandstones and conglomerates (Sentürk et al., 1998). Because of the scarcity of outcrops adjacent to the fault trace we studied fault-related deformation patterns within the

[1] For interpretation of the references to colour in this text, the reader is referred to the web version of this article.

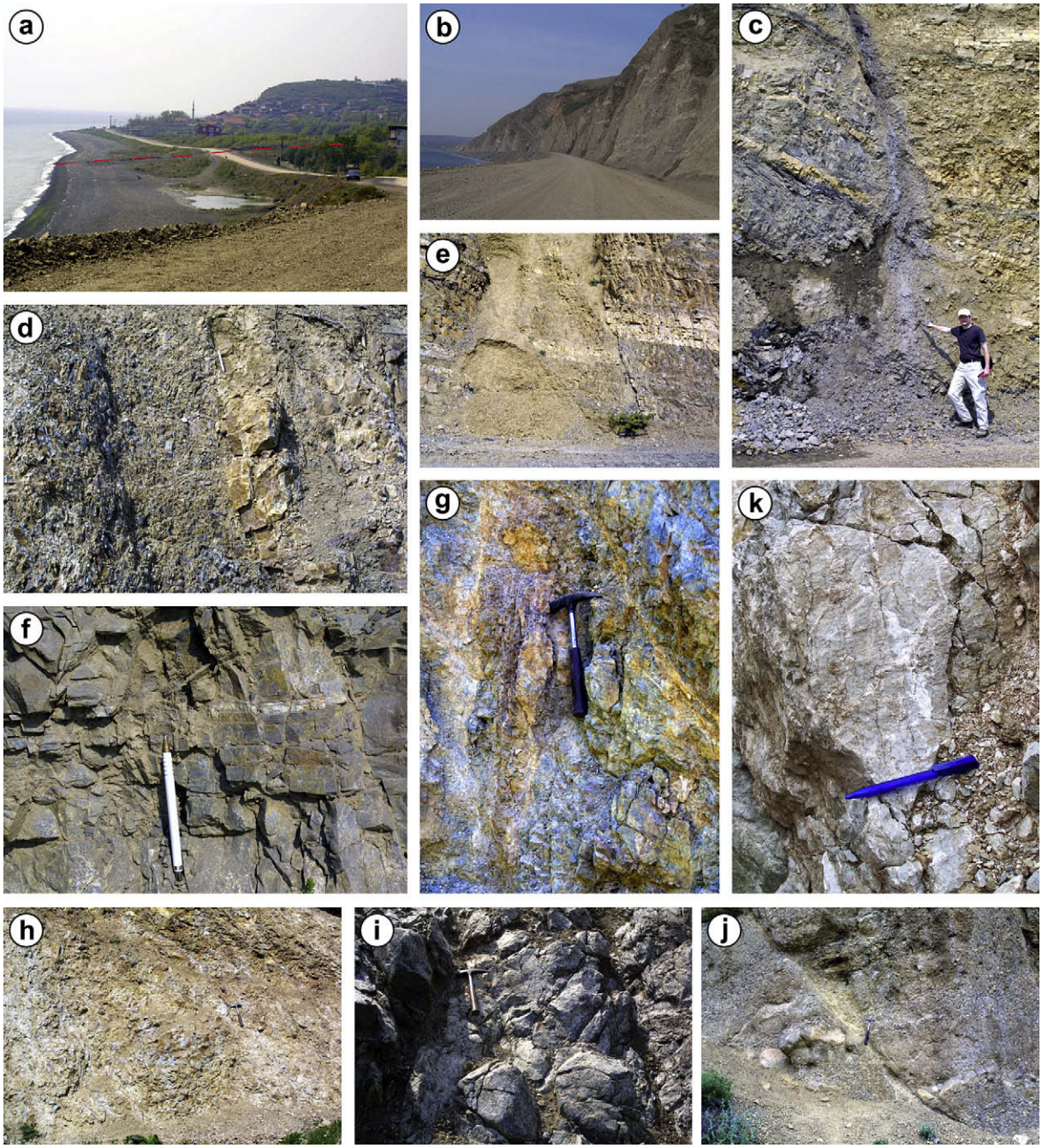

Fig. 4. Outcrop views and photographs of fault-related deformation structures in all four investigated locations. (a) View south–southwest across the main trace of the Ganos fault. The red dashed line is the approximate location of the fault trace (about 22 m offset along the coastline, Altunel et al., 2004). (b) View south-west along the well-exposed Gaziköy Formation. (c) Normal fault in Eocene turbidites with fault-related friable breccias. (d) Gradual transition from slightly deformed host rock to a cataclasites. (e) Field photograph showing erosion and discoloration of fault rocks. (f) Small horizontal quartz vein in Eocene turbidite. (g) Center of the fault breccia zone with altered and discoloured shear bands. (h) Assumed fault core with unconsolidated alteration material. (i) Serpentinites imbedded in a Tertiary olisthromal sequence. (j) Normal fault within the Eocene-Oligocene sequence. (k) Limestone with veins, striations and stylolites. Notice that the direction of stylolitic columns coincides with striation directions.

Gaziköy formation along the well-exposed coastline north of the fault trace (Figs. 1b and 4b). This half profile extends from 700 m distance to the fault to about 2000 m to NNE.

The sedimentary sequence shows numerous small normal faults (Fig. 4c), ranging from ~10 cm to more than 10 m in length, which cut through the folded shale- and siltstone layers dismembering F_1 folds. Two sets of faults dominate the fault patterns; one set with some scattering in orientation comprises NW–SE to NNW–SSE trending normal faults and is more abundant than the other set which is composed of E–W trending faults (Fig. 5a–c; see also Hancock and Erkal, 1990; Okay et al., 1999). Hancock and Erkal (1990) described the normal faults as second-order products generated during transpression along and across the GF zone.

Outside the profile (i.e. at greater distance from the fault trace) normal faults are fewer, suggesting that their formation is related to faulting activities (Okay et al., 1999). However, along the profile a significant decrease of faulting intensity (damage) with increasing distance from the fault trace was not observed (Fig. 5d). Subsidiary normal faults reveal a transition from fractured host rocks (fracture spacing >20 cm) to cataclasites (Fig. 4d). The cataclastic zones,

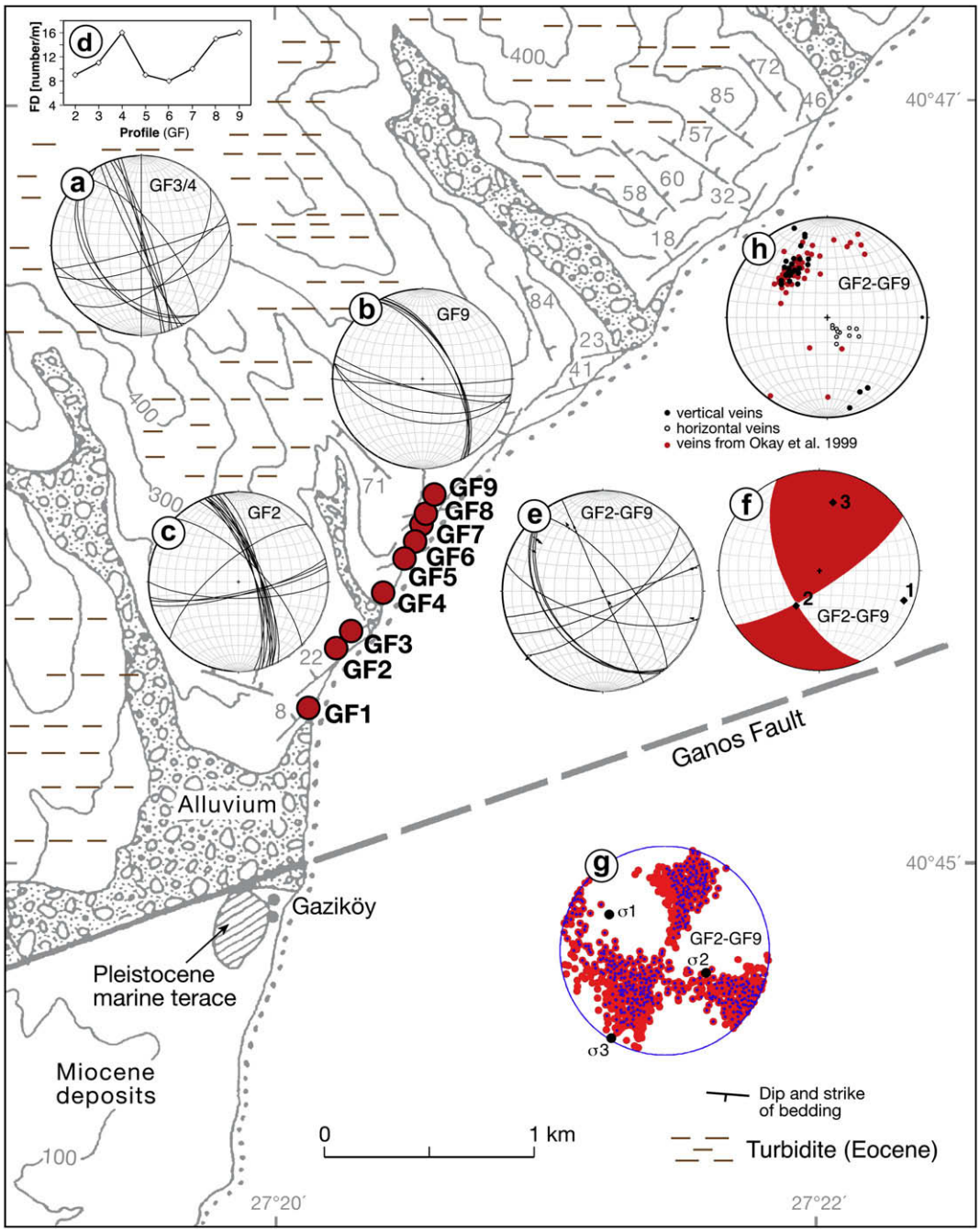

Fig. 5. Structural map of the coastal section northeast of Gaziköy (*study-area A*; slightly modified after Okay et al., 1999; GF1–GF9 = locations). (a–c) Stereonets show orientation data for normal faults. (d) Number of fractures, subsidiary faults and veins per meter. (e) Fault planes with striation directions. (f) Fault plane solution the white quadrant contain the compression axis (1) and the red quadrant the extension axis (3). (g) Results of stress-tensor inversion containing 10 fault plane solutions. Bold black dots represent the best fitting orientations for the three principle stresses (σ_1 = maximum compressional stress, σ_2 = intermediate, σ_3 = minimum). Small and large dots represent the σ_1 and σ_2 confidence intervals. (h) Poles to the veins (h). (For interpretation of the references to colour in this figure legend, the reader is referred to the web version of this article).

ranging in thickness between 20 and 30 cm, consist of sediments that are friable and highly fractured parallel to the minor faults. Alteration processes are widespread causing erosion and visible discoloration of fault rocks (Fig. 4e). In addition, we observed few fault planes with subhorizontal striations exhibiting different directions (Fig. 5e). Superimposed striae indicate that they are older than normal faults. Their composite fault plane solution reveals strike-slip faulting with a reverse component of slip (Fig. 5f). The principal stress axes derived from stress-tensor inversion indicate a subhorizontal ESE–WNW direction for the largest principal stress (σ_1). However, the confidence intervals are comparatively large and partly overlap, indicating that the stress directions are not well resolved (Fig. 5g). In the turbidites of the Gaziköy formation, veins trend parallel or at a low angles to the fault trace with moderate dip angles to SE (Fig. 5h; see also Okay et al., 1999). The veins vary between 2 mm and 1 cm in width and are filled with quartz and different types of calcite cement (Fig. 4f, see Section 5.1).

In study-area B, the GF continues southwestward through the Ganos mountains but is mostly covered by young quaternary sediments. Along the fault zone, weakly folded Eocene shales and siltstones of the Gaziköy Formation are overprinted by a fault-related brittle deformation. Pervasively brecciated sediments

comprise cataclasites and a zone of gouge (altered) material. The gouge zone contains small subsidiary shear zones (Fig. 4g). This area is referred to as the fault zone core. The shear zones strike northwest and dip at steep angles to the NE or SW (Fig. 6a). Fault-related veins are extremely rare (Fig. 6a). They were formed sub-parallel to the GF trace.

Study-area C is in a region where the GF was found to consist of two main branches (Okay et al., 1999). The northern branch is partly exposed revealing a transition from an altered cataclasite (fault core) to fractured Eocene shales (fault damage zone; Fig. 4h). Rare calcite veins trend parallel or at low angle to the fault trace. Fault orientations in GF15 scatter more than those in area B (Fig. 7a). Fault sets with NW–SE, ENE–WSW and N–S trending faults are dominant. The composite fault plane solution shows a strike-slip regime with subhorizontal NW–SE shortening and NE–SW extension (Fig. 7b). Results of the stress-tensor inversion show no clear separation between the principal stress axes (Fig. 7c). The fault is also exposed in a Tertiary sandstone-siltstone sequence that contains clasts of serpentinites (GF16; Fig. 4i) and middle Eocene reef limestones (GF18; Okay et al., 1999). Small subsidiary faults strike consistently NNE–SSW and dip at moderate angles to NNW (Fig. 7d). The fault plane solution suggests a predominant normal faulting mechanism (Fig. 7e) and the inversion result reveals a well-constrained NNW–SSE orientation for the maximum principal stress (σ_1; Fig. 7f).

Toward the west (*study-area D*), the fault splits into at least three branches with a change in deformation style from dominantly strike-slip and/or transtensional faulting in the east to more transpressional faulting and thrusting in the west. NE-trending normal faults are found in the interbedded sandstones and conglomerates within the Eocene–Oligocene sequence (GF19; Fig. 4j) whereas the Eocene limestone outcrops (GF20) exhibit compressive structures (Fig. 8a). Calcite veins in conglomerates and sandstones are rare but fault rocks within the limestone outcrops are partially cemented (Fig. 4k). In these outcrops, two faulting events could be established by superimposed striae. The older

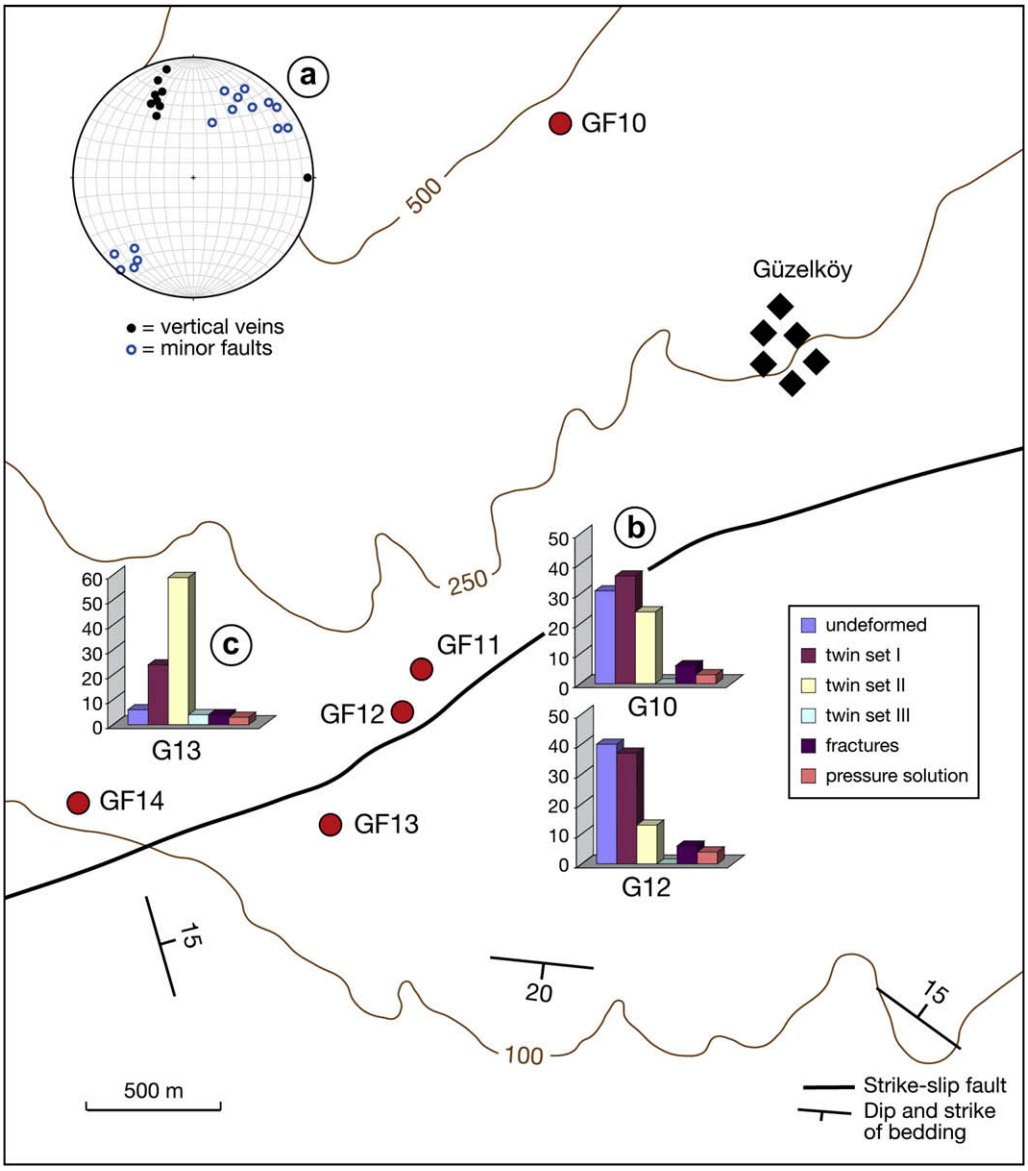

Fig. 6. Structural map of *study-area B*; slightly modified after Okay et al., 1999; GF = locations, G = sample number. (a) The stereonet shows poles to minor faults and vertical veins. (b and c) Columns represent the normalized percentages of selected microstructures in vein cement (twins with one (I), two (II) or three (III) sets, fractures and pressure solution seams) and undeformed grains.

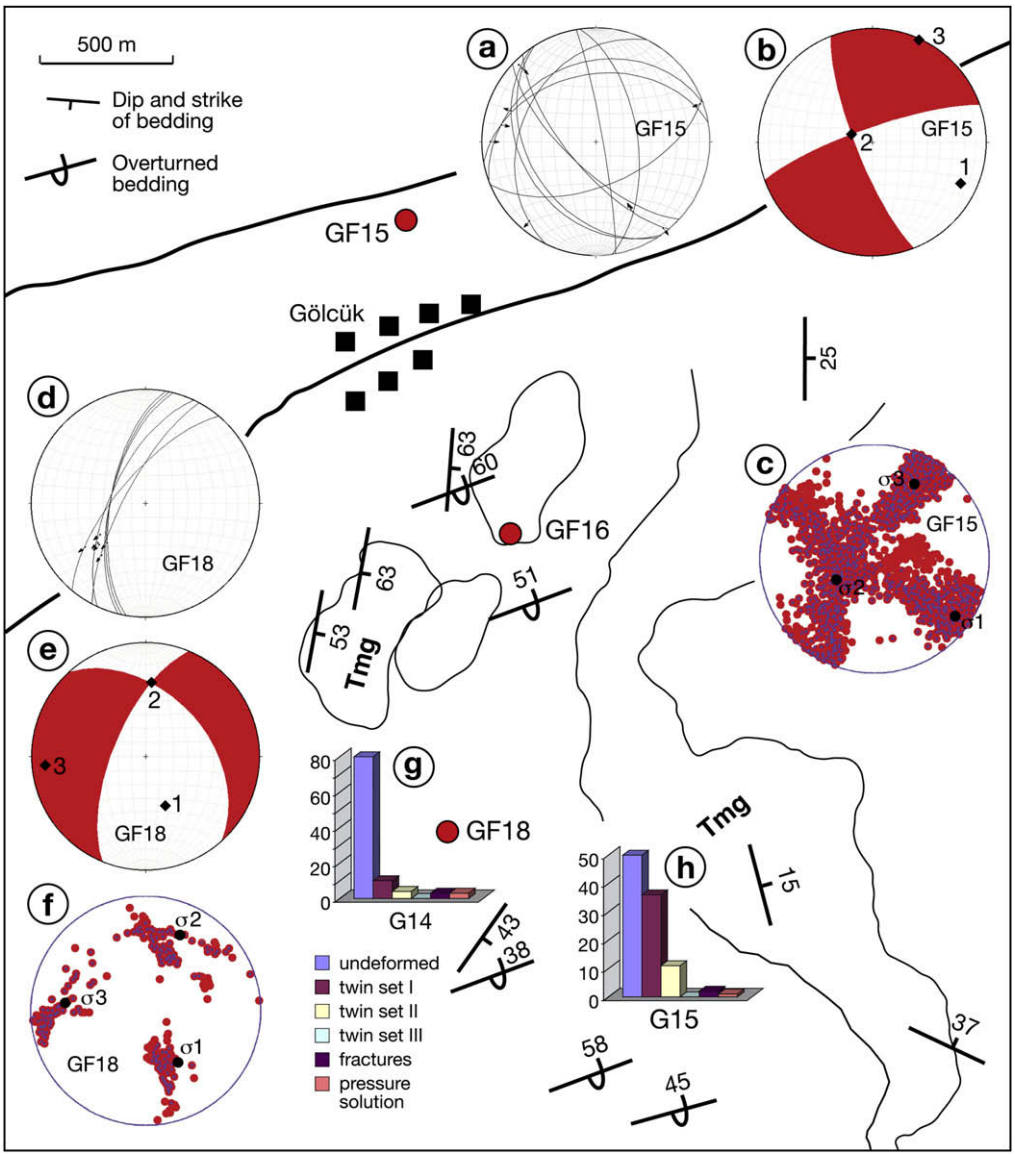

Fig. 7. Structural map of *study-area C*. Stereonets show orientation data for 16 fault planes with striation directions (a and d), fault plane solutions (b and e) and results of stress-tensor inversion (c and f). Percentages of microstructures (g and h). For further explanations see Figs. 5 and 6.

event is documented by two main strike-slip fault sets (Fig. 8a). The fault plane solution shows pure strike-slip faulting (Fig. 8b) and the stress inversion results exhibit a well-defined E–W trending direction of σ_1 whereas σ_2 and σ_3 overlap in their confidence intervals (Fig. 8c). The younger fault set contains few WNW–ESE trending faults with a thrust component (Fig. 8d and e).

The summarized kinematic results for the entire fault reveal a pure strike-slip regime (Fig. 9a). The stress-tensor inversion shows a relative stress magnitude of 0.66 indicating that there is no clear separation between the intermediate (σ_2) and the maximum (σ_1) principal stresses and both may have a similar trend (NW–SE). In contrast a well-constrained NE–SW orientation for the minimum principal stress (σ_3) at shallow dipping angle could be identified (Fig. 9b).

Furthermore, our results for the entire fault are roughly compatible with the fault plane solution derived from microseismic activity at the GF (Fig. 9c) and with the W–E (WNW–ESE) maximum horizontal compressive stress direction obtained from the regional (world) stress map (Heidbach et al., 2008). This suggests that directions of the paleostresses are similar to the present stress field.

5. Microscopic observations

Microscopic observations have been performed prevailing in calcite and/or quartz (vein) cement because the occurrence of deformation mechanisms is grain size dependence. We used cathodoluminescence (CL) microscopy to discriminate different vein cements. Fluid inclusion (FI) data from veins was used to estimate the *P–T* conditions prevailing during faulting. All veins investigated in this study are fault-related as suggested by their abundance, which progressively increase toward the GF, and by their orientation with respect to the fault.

5.1. Cathodoluminescence characteristics

Variations in the cathodoluminescence (CL)-colours are usually attributed to a different trace element composition of the original

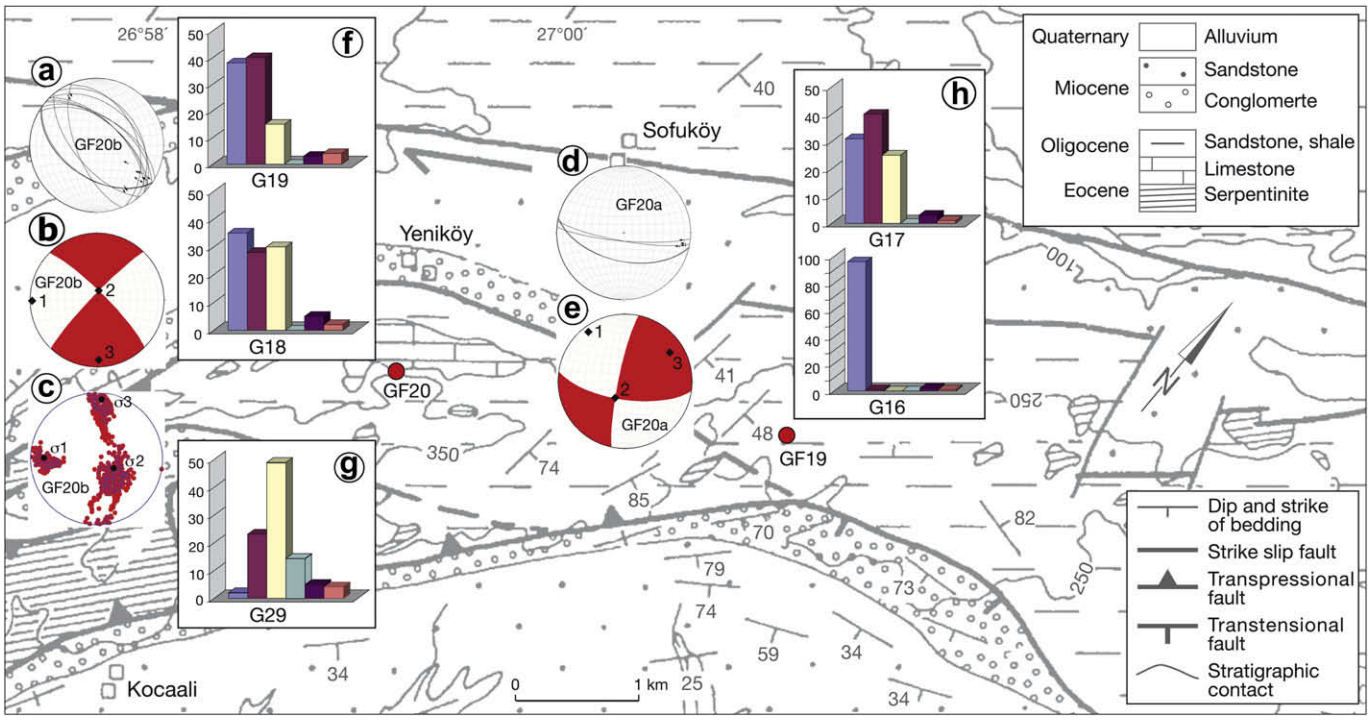

Fig. 8. Structural map of *study-area d* (slightly modified after Okay et al., 1999). Stereonets show orientation data for 17 fault planes with striation directions (a and d), fault plane solutions (b and e) and results of stress-tensor inversion (c). Percentages of microstructures (f and g). For further explanations see Figs. 5 and 6.

fluids from which the cement precipitated. Using CL-microscopy, several calcite and quartz cement generation could be detected that are invisible in ordinary light. Along the GF, fault rock samples show a significant luminescence contrast between fracture cement and fine-grained fault matrix. In fault breccia samples, the calcite cement luminesces red to orange, whereas fault matrix and rock fragments do not luminesce.

At least six different episodes of cementation could be identified (Table 1). The oldest calcite cement (generation I) with red to dark orange CL-colours is strongly deformed with up to three twin sets (Fig. 10a and b). Few twins are modified by dynamic recrystallization (see below). This cement type could only be detected in two samples of *study-area A and D* (Table 2). The oldest quartz cement (generation II; *study-areas A and B*) luminesces blue (Fig. 10c and d). These *short-lived blue* colours of quartz cement indicate a hydrothermal origin (Götze et al., 2001). Generation II-quartz cement is partly replaced by blocky calcite cement of generation III (*study-areas A, B and D*). Generation III-calcite, with similar CL-colours as generation I, is intersected by younger vein-calcites with bright orange to yellow luminescence colours (generation IV, in all sub-areas; Fig. 10e and f). The younger vein-calcites of generation IV are weakly deformed with straight and thin twin lamellae (<1 μm). In two fault rock samples of *study-area A and D*, some fractures were healed by calcite cement, which is not twinned or fractured (generation V; Tables 1 and 2), indicating that healing processes outlasted brittle faulting. This cement type does not luminesce. Undeformed and likewise non-luminescent quartz grains in one sample of *sub-area A* have been identified as the latest generation (Generation VI, Fig. 10g and h, Tables 1 and 2).

Variations in the CL-colours of calcite cements are attributed to the initial trace element composition in the fluid and/or to changes in redox conditions at the site of precipitation (Meyers, 1974). Luminescent calcite cements may be precipitated under meteoric phreatic to deep burial conditions (Meyers, 1978). The non-luminescent calcite cement implies oxidizing conditions during shallow precipitation or reducing burial conditions with high Fe contents and little Mn (Verhaert et al., 2004).

5.2. Microstructures

5.2.1. Methods

At low deformation temperatures (<300 °C) mechanical e-twinning is an important deformation mechanism in calcite. The width, density and the number of twin systems activated were used to estimate deformation temperatures (Burkhard, 1993; Ferrill, 1998; Ferrill et al., 2004). Burkhard (1993) and Ferrill et al. (2004)

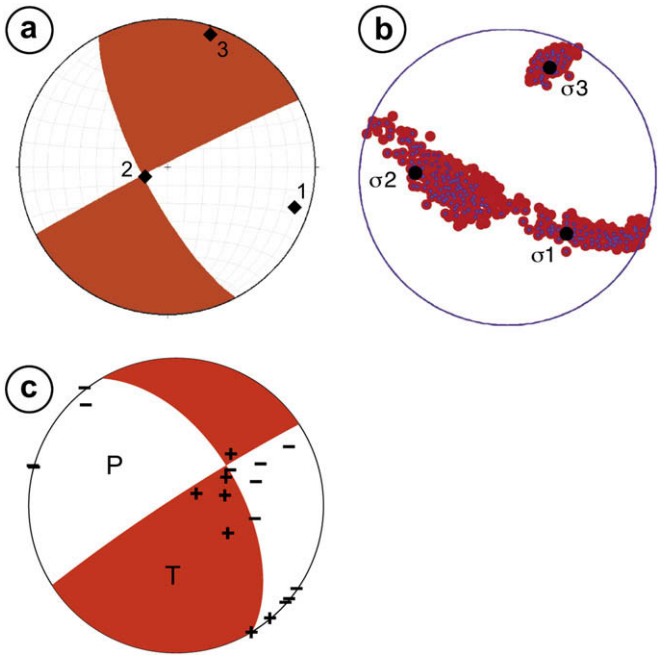

Fig. 9. Summary of the results of the kinematic analysis. (a) Fault plane solution for the entire database. (b) The stress-tensor inversion for the entire paleostress database containing 44 fault plane solutions. For further explanations see Fig. 5. (c) A cumulative fault plane solution for each microseismic cluster based on P-wave polarities.

Table 1
Description of thin sections, with a note on mineralogy, cement type, CL observations, microstructures and derived deformation conditions (FI = fluid inclusion).

Stage of cementation	Sub-area	Cement composition	Cement type	CL observation	Deformation-structures	T,Δσ twins	*P–T* FI
VI	A	Quartz	Small grains	Do not luminesce	Completely undeformed		
V	A, D	Calcite	Elongated fibrous calcite	Do not luminesce.	Completely undeformed	Sub-surface conditions?	
IV	A, B, C,D	Calcite	Blocky cement	Bright CL colours	Weakly deformed, thin twin lamellae	<170 °C <20 MPa	70–140 °C <50 MPa
III	A, B, D	Calcite	Mosaic cement	Orange CL colours	Thick twin lamellae, partly curved	150–250 °C 50–80 MPa	70–170 °C <50 MPa
II	A, B	Quartz	Blocky cement	Blue CL colours	Fractured		170–250 °C 40–120 Mpa
I	A, D	Calcite	Blocky and fibrous cement	Dark orange CL colours	Thick. curved twins: start of dynamic re- crystallization.	200 ≥ 250 °C 80–100 MPa	

published a classification of twins in relation to their appearance in thin sections. They suggest that twin width increase with increasing temperatures in naturally deformed coarse-grained calcite. Thin twins (<1 μm) dominate below 170° and thick twins (>5 μm) dominate above 200 °C, whereas above 250 °C dynamic recrystallization becomes more important. However twin thickness enabled only a rough temperature estimate (Janssen et al., 2007a). Here, we use a combination of a (twin-) temperature gouge and fluid inclusion data (see below).

In addition, two approaches based on calcite twins can be used to estimate differential stress magnitudes (Δσ). One approach is based on twin density (Rowe and Rutter, 1990) and the other on the percentage of calcite grains with one, two or three twin sets (Jamison and Spang, 1976). For low-temperatures (<250 °C), the Rowe and Rutter method tends to overestimate the differential stresses (Ferrill, 1998). For the purpose of this work, we used the Jamison and Spang method only, because of deformation temperatures estimated from fluid inclusion data in calcite are <250 °C (see below). The basic criteria of this method (e.g. homogeneous stress distribution in the aggregate, random orientation of c-Axes, and a threshold value of critical resolved shear stress) are fulfilled in our samples. However, within GF twins may record peak stresses during rapid slip movements or seismic shocks rather than being representative of the fare-field stress of interest (Burkhard, 1993). We further calculated the normalized percentages of selected microstructures in vein cement (twins with one, two or three sets, micro-fractures and pressure solution seams).

5.2.2. Results

Within *study-area A*, a microstructural analysis was carried out on calcite vein samples, which were collected along a traverse perpendicular to the fault. Twins, micro-fractures and pressure solution features were observed in most calcite grains where twinning is the dominant deformation mechanism (Fig. 11). The twinned crystals display one two or three sets of straight or bent twins. In one sample (G9, Table 2; cement generation I) some thick and patchy twins are modified by dynamic recrystallization. Similar to the meso-structural deformation patterns, microstructures indicate no increase in deformation intensity toward the fault trace. Instead, we observed considerable differences in deformation intensity between selected vein samples of one outcrop (cement generation I–V), suggesting a time-variant deformation behavior. Deformation temperatures derived from the appearance of twins vary between <170 and ≥250 °C, and the maximum differential stress derived from the percentage of twinned grains differs between <20 and 100 MPa (Table 1).

The percentages of vein-calcites in *study-area B* (cement generation III; Fig. 6b and c) that are twinned, fractured and affected by pressure solution are in a similar range as described for the *study-area A*. Up to 80% of all grains in thin section display one or more twin sets. Less than 5% of the grains show pressure solution features (saturated or interpenetrated grain–grain contacts). Deformation temperature ($T = <170–250$ °C) and paleo-differential stresses estimated from vein-calcites ($\Delta\sigma = <20–80$ MPa) are similar as in *study-area A* (Table 1).

Calcite veins in *study-area C* are rare and thin sections of generation IV-calcite cement reveal a smaller amount of microstructures than in samples from area A and B (Table 2; Fig. 7g and h). Less than 5% of grains are fractured or show sutured grains indicative for pressure solution. Also twinning (twin set I and II) is less abundant (<50%) than in *study-areas A* and *B*. The straight and thin twin lamellae (<1 μm) suggest deformation at low-temperature (<170°). Applying twinning paleopiezometry, we estimated differential stress magnitudes <20 MPa (Table 1).

Microscopic observations of calcite vein cements in *study-area D* display significant differences in deformation intensity and deformation conditions (cement generation I and III–V; Fig. 8f and h, Table 1). In samples G29, G19, G18 and G17 the deformation intensity is higher or at least comparable with the deformation within the sub-areas A and B. However, in sample G16, cement-crystals are not twinned or fractured (Table 2, Fig. 8h). Also deformation temperatures and differential stress magnitudes differ markedly between the selected samples. In sample G19 (cement generation I) both, the appearance of twin sets (bent and thick twin lamellas) and features of dynamic recrystallization indicate deformation temperatures >250 °C (Table 1). The derived paleo-differential stress varies between 80 and 100 MPa. On the other side of the spectrum, completely undeformed calcite vein cement (G16; generation V) indicates that the healing processes (cementation) outlasted brittle faulting.

In summary, vein samples from all sub-areas exhibit different generation of calcite cement that were formed at varying temperatures and differential stress magnitudes. Spatial variations of microstructures toward the fault have not been observed (Fig. 11). The dominant deformation mechanisms like micro-fractures and deformation twinning are widely distributed.

5.3. Fluid inclusions and their significance

5.3.1. Methods

Fluid inclusions, suitable for the study were found in veins of three quartz- and four calcite-bearing samples from study-area A, B and D (Table 2). All veins are fault-related as suggested by their orientation with respect to the fault. For investigation of inclusions, 0.1–0.2 mm thick wafers, polished on both sides, were prepared. The fluid inclusions were studied at temperatures between −190 and +500 °C using the Fluid INC. heating-freezing stage. The accuracy of temperature measurements was about ±0.5 °C in the low-temperature range (−190 ± 50 °C) and ±2 °C in the high temperature range (100–500 °C).

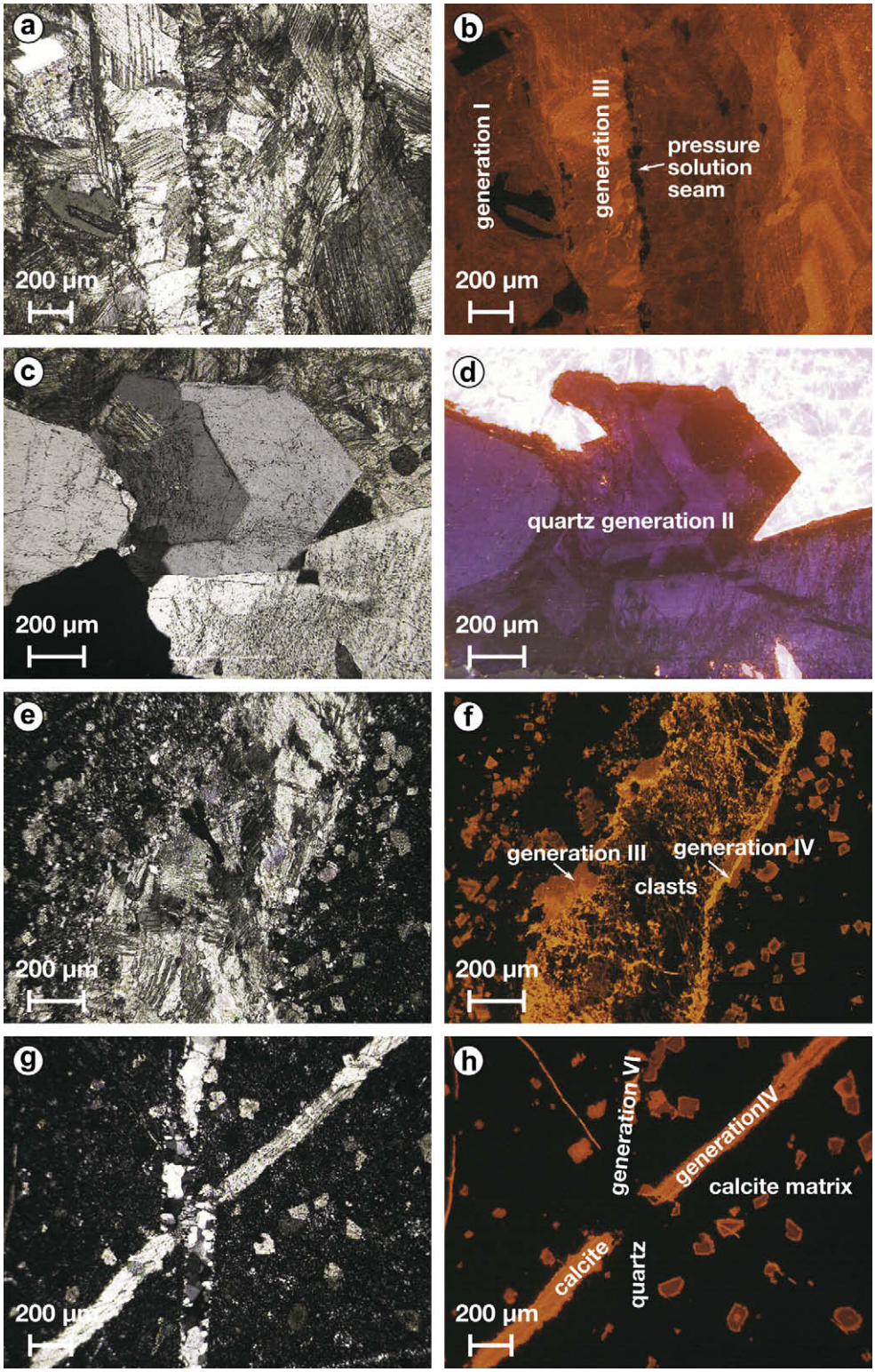

Fig. 10. Photomicrographs of microstructures under crossed nicols (left) and CL photographs (right) of the same region. (a and b) Strong deformed vein cement. Different calcite generations (I and III) are visible under CL. (c and d) Quartz (Generation II) is replaced by calcite. (e and f) Fault matrix with two generations of calcite veins (III). (gand h) Intersections of veins. The older calcite vein (generation III) is dissected by the youngest quartz vein generation (VI).

The analysis of gases in fluid inclusions was performed by use of a confocal Raman microspectrometer (Renishaw system 1000, Institute of Earth Sciences, Jerusalem) equipped with a triple monochromator and a CCD detector. The green (514.5 nm) polarized light of an argon laser beam (250 mW power) was used for excitation. The scattered light was collected through the objective ($\times$50) of an Olympus optical microscope. Entrance slits of 100 µm gave a spectral line width of about 3.5 cm^{-1}, with a spectral resolution of less than 1 cm^{-1}, and a frequency reproducibility of the same order. All investigations were

Table 2
Sampling area and description, stages of cementation and methods used.

Sample-Nr	Sub-area	Sample desription	Stage of cementation	Microstructur -analys	Stable isotpes	Fluid inclusions
G1	A	Sandstone + Cc-vein	III	X	X	
G2	A	Sandstone + Cc-vein	III	X	X	
G3	A	Sandstone + Cc-vein	IV	X	X	
G4	A	Sandstone + Cc-vein	IV	X	X	
G5	A	Sandstone + Cc-vein	III	X	X	
G6	A	Sandstone + Cc-vein	III	X	X	
G7	A	Sandstone + Cc-vein	V	X	X	
G8	A	Sandstone + Qz-vein[a]	II		X	X
G9	A	Sandstone + Cc-vein	I	X	X	
G10	B	Sandstone + Qz-vein	II		X	X
G11	B	Altered material			X[c]	
G12	B	Sandstone + Cc-vein	III	X	X	
G13	B	Sandstone + Cc-vein	III	X	X	
G14	C	Limestone + Cc-vein	IV	X	X	
G15	C	Limestone + Cc-vein	IV	X	X	
G16	D	Sandstone + Cc-vein	V	X	X	
G17	D	Limestone + Cc-vein	III	X	X[b]	
G18	D	Limestone + Cc-vein	III	X		X
G19	D	Limestone + Cc-vein	I	X		X
G20	A	Sandstone + Cc-vein	III	X		
G21	A	Sandstone + Cc-vein[b]	IV + VI	X		
G22	A	Sandstone + Cc-vein	III	X		
G23	A	Sandstone + Cc-vein	III	X	X[c]	
G24	A	Sandstone + Qz-vein	II		X[c]	X
G25	A	Sandstone + Cc-vein	III	X	X[c]	
G26	B	Sandstone + Cc-vein	IV	X	X[c]	
G27	B	Sandstone + Cc-vein	III	X	X	
G28	D	Sandstone + Cc-vein	IV	X	X	
G29	D	Limestone + Cc-vein	III	X	X	
G30	D	Limestone + Cc-vein	IV	X	X	X
G31	D	Limestone + Cc-vein	III	X	X	
G32	D	Limestone + Cc-vein	III	X		

[a] +Cc-vein.
[b] +Qz-vein.
[c] Intensity to low.

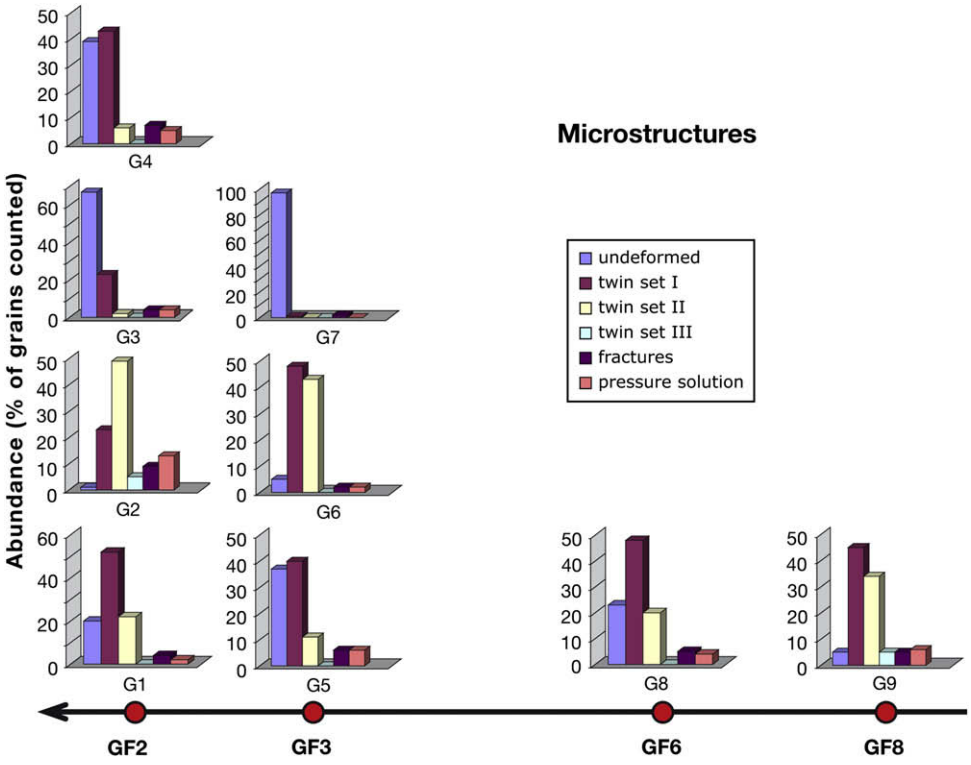

Fig. 11. Results of microstructural analysis in study-area A along a half profile extending from 700 m distance to the fault to about 2000 m to NNE. For further explanation see Fig. 6.

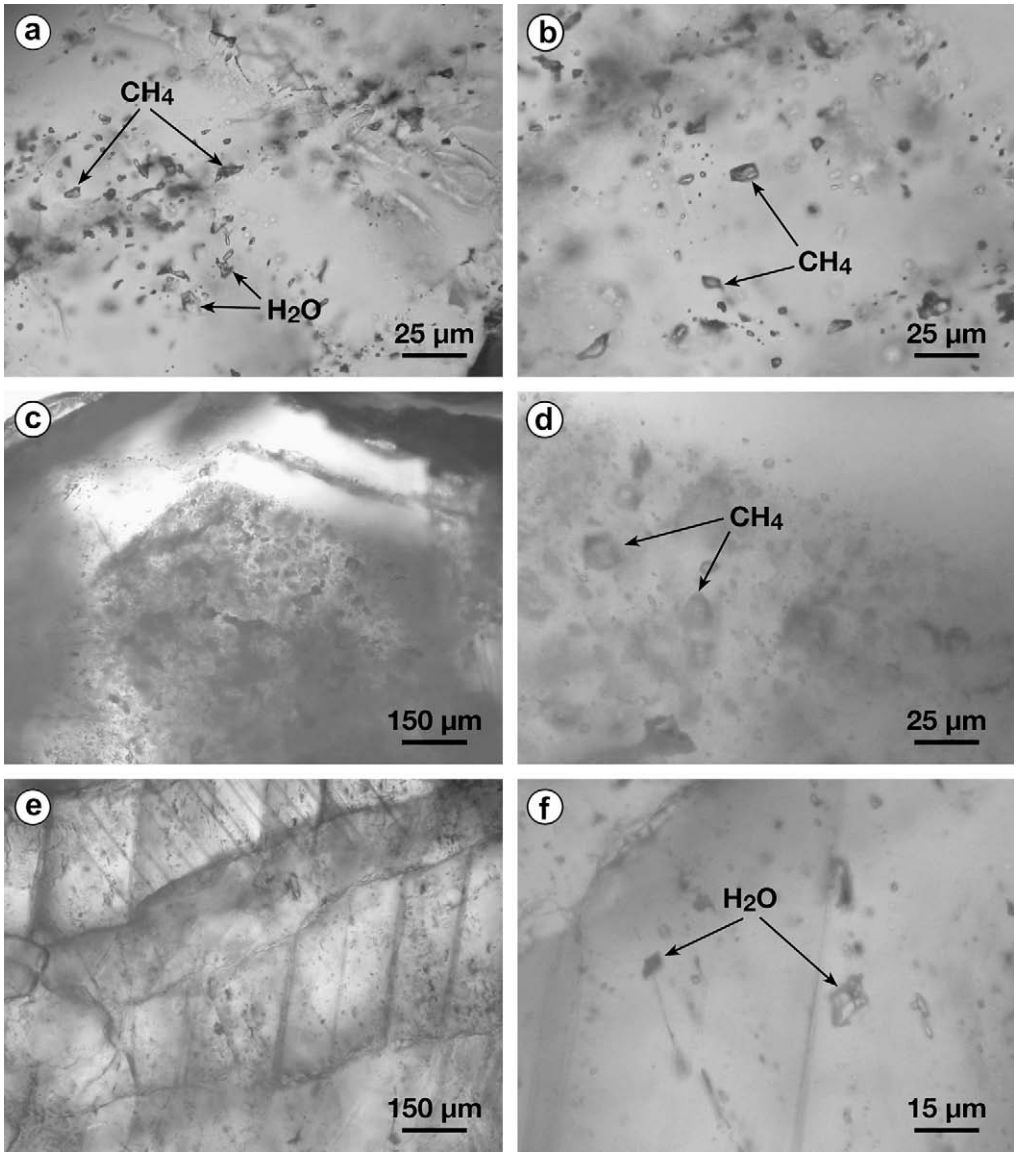

Fig. 12. Fluid inclusions in quartz and calcite veins. (a and b) Pseudosecondary CH_4 and aqueous inclusions, sample G8; (c) and enlarged (d) CH_4 inclusions in a core of chevron quartz, sample G24; (e) and enlarged (f) primary aqueous inclusions in calcite, sample G18.

performed at room temperature in air. The spectral acquisition time was 30 s.

5.3.2. Results

Fluid inclusions were found in three quartz veins of samples of cement generation II (G8, G10 and G24; Tables 1and 2). These are gaseous and aqueous inclusions (Fig. 12a–f), their size ranges between 10 and 20 µm. The inclusions are of primary and pseudo-secondary origin. In one sample (G24), primary gaseous inclusions are located in a core of chevron quartz (Fig. 12c and d). The inclusions show homogenization mainly into the liquid phase between −92 and −81 °C (Fig. 13a). In one sample (G10), such inclusions show homogenization into the vapor phase. The behavior of these gaseous inclusions during heating-freezing runs suggests that inclusions are methane-bearing. Raman spectra confirmed that these inclusions are filled with pure methane (Fig. 13b). Aqueous inclusions are relatively rare and often occur between the pseudo-secondary methane-bearing inclusions. They are composed of a liquid and a vapor phase (the vapor liquid ratio is between 10 and 20 vol. %) and show homogenization into the liquid phase between 150 and 185 °C (Fig. 13c). The first melting temperature (T_{fm}) was observed between −3 and −2 °C, the final melting temperature (Tm_{ice}) between −1 and 0 °C. These microthermometric data suggest sodium-potassium HCO_3^- and/or SO_4^{2-} solutions (Borisenko, 1977) with salinity up to 3.0 eq. wt% NaCl (Bodnar and Vityk, 1994).

Aqueous inclusions were found in four calcite samples of cement generation I (G19), III (G18) and IV (G30/1 and G30/2). Inclusions are of primary and pseudo-secondary origin; their size is −10 µm. These are two phase (liquid and vapor) inclusions. The vapor liquid ratio is about 10–20 vol. %. Homogenization is into the liquid phase and mainly between 70 and 170 °C (Fig. 13c). T_{fm} is ∼ −2 °C and Tm_{ice} between −1 and 0 °C. These aqueous inclusions are similar to the aqueous inclusions present in quartz. In one sample (G18), another type of aqueous inclusions was observed. Although the range of Th of these inclusions is similar to inclusions in the other calcite samples, T_{fm} occurs at −17 and −8 °C and Tm_{ice} is between −4 and −0.5 °C. These are likely NaCl-rich solutions with salinity up to 6.5 eq. wt% NaCl (Bodnar and Vityk, 1994).

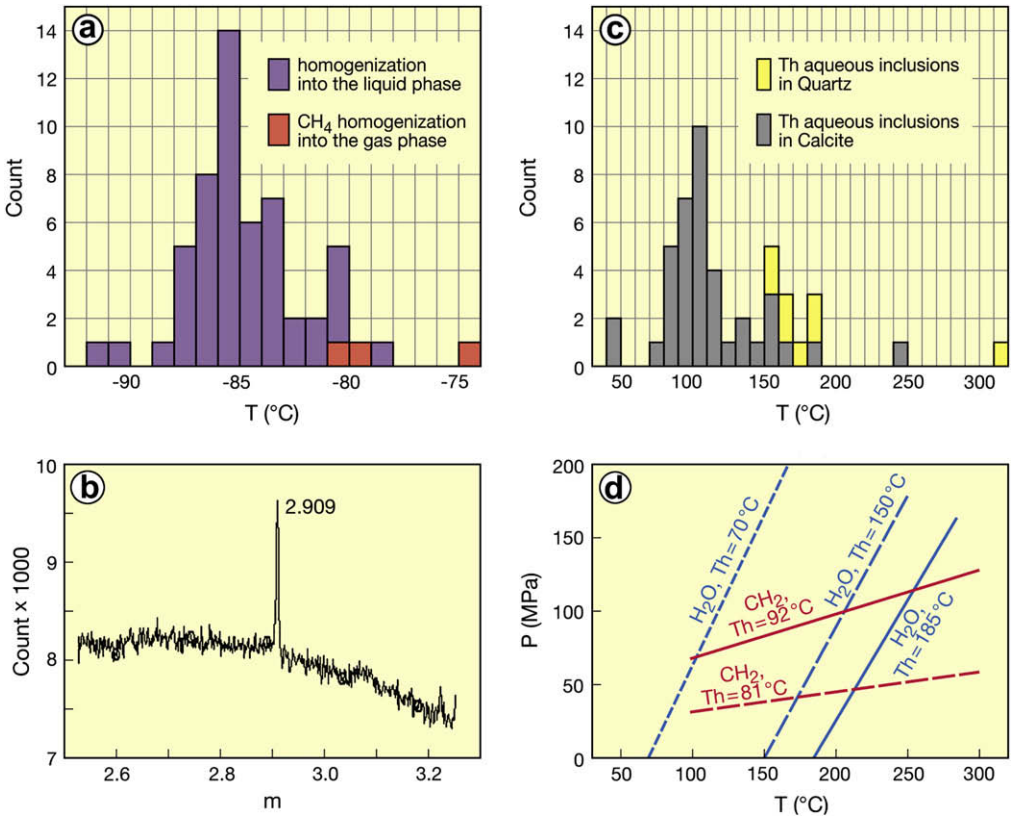

Fig. 13. Diagrams of fluid inclusion data. (a) The temperature of homogenization of CH_4 inclusions. (b) Raman spectrum of CH_4 inclusion, sample G8. (c) The homogenization temperature of aqueous inclusions. (d) Typical isochores of CH_4 and aqueous inclusions and *P–T* conditions of inclusion trapping.

The fluid inclusion study unambiguously shows that CH_4 inclusions are earliest type of inclusions in studied quartz veins (Fig. 12c). The aqueous inclusions were trapped during the continued quartz growth. Most aqueous inclusions are associated with CH_4 inclusions in growth zones and absent in secondary trails. Such characteristic occurrence of aqueous and CH_4 inclusions is a good indication of the simultaneous trapping of both inclusion systems. It is likely that the same aqueous system (mainly sodium-potassium-bicarbonate-sulfate solution with salinity up to 3 eq. wt% NaCl) caused calcite growth. Other aqueous inclusions with a sodium-chlorine composition and salinity up to 6.5 eq. wt% NaCl likely reflect a new pulse of fluid into the fault zone.

The microthermometric data on fluid inclusions were used for the determination of *P–T* conditions of fluid inclusion trapping and quartz vein formation (Fig. 13d). The intersection of typical CH_4 isochores (according to Duan et al., 1996; Bakker, 2003), with isochores of the aqueous inclusions (according to Bodnar and Vityk, 1994) in quartz, determines the possible range of pressure and temperature during the formation of the quartz veins. Quartz could have precipitated at a temperature between 170 and 250 °C and pressures between 40 and 120 MPa. Calcite vein growth occurred at temperature decreasing from 170 °C to 70 °C, at pressures likely below 50 MPa.

6. Stable isotopes

6.1. Sampling and analytical methods

Samples of calcite veins, carbonate-bearing host rocks and limestone-host rocks were taken from several locations of the four sub-areas investigated in this study (Fig. 1). Small core samples of veins and surrounding host rocks were drilled from polished slabs using a jeweller's microdrill. Stable isotope analyses were performed using a continuous-flow technique consisting of a ThermoFinnigan GasBench II linked to a DELTA^{plus} XL mass spectrometer (GFZ Potsdam). The 1σ precision for $\delta^{13}C$ and $\delta^{18}O$ is better than 0.08‰. The $\delta^{18}O$ values refer to Vienna-Standard Mean Ocean Water (V-SMOW), and the $\delta^{13}C$ values to the Cretaceous Peedee Belemnite (PDB). In some host rock samples, the isotopic intensity was too low so that only veins were measured.

6.2. Results

The carbon and oxygen-isotope compositions for all fault-related calcite veins and host rock samples are shown in Fig. 14a. A comparison for all $\delta^{18}O$ and $\delta^{13}C$ values of sub-area A, B, C and D shows that values overlap and are not separated into distinct populations. If we only consider host rock samples, then we can separate host rocks (carbonate-cemented sandstones) of sub-area A and B from limestone-host rocks of sub-area C and D. Furthermore, host rock and veins have different isotopic compositions independent from their regional provenance (Fig. 14a). However, $\delta^{18}O$ and $\delta^{13}C$ values of calcite veins scatter significantly more than host rock samples (Fig. 14b). The oxygen and carbon isotope values for host rock samples reveal a total range of 18.5–24.8‰ and −4.88‰ to 1.75‰, respectively. The values of vein calcite show a wider range of $\delta^{18}O$ values, from 12.7‰ to 23.9‰, and $\delta^{13}C$ values from −7.27‰ to 2.13‰. The results reveal two different trends. Oxygen data from strongly deformed calcite veins (cement generation I and III) are significantly depleted with up to 8,7‰ difference (sample G9) between host and vein, whereas the $\delta^{13}C$ values of those samples vary in a narrow range (Fig. 14b). For some weakly deformed veins (cement generation IV and V), the oxygen and carbon isotope values are similar to those of related host rocks. The undeformed

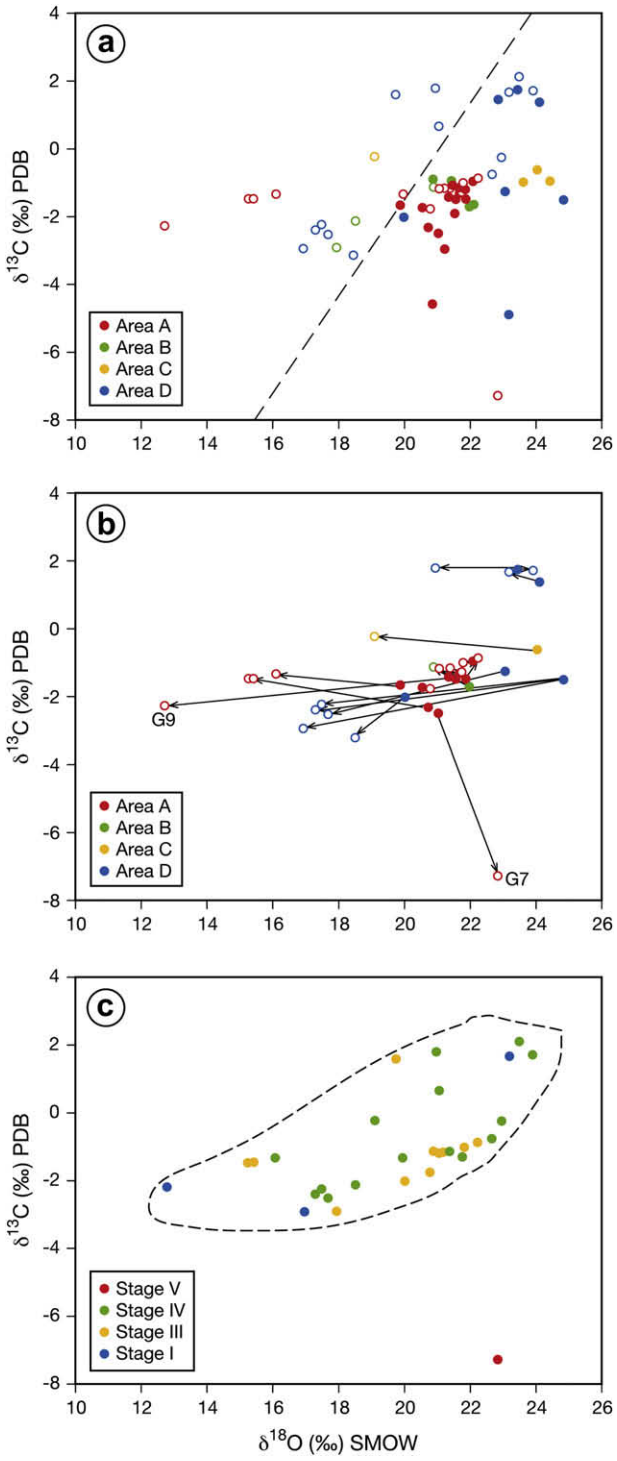

Fig. 14. Diagrams of stable isotope data. (a) Cross-plot of the $\delta^{18}O$ and $\delta^{13}C$ of all carbonate samples (open circles = calcite veins; filled circles host rock). (b) Relations of $\delta^{18}O$ and $\delta^{13}C$ values between host rocks and veins. (c) $\delta^{18}O$ and $\delta^{13}C$ values of veins related to different calcite cement generation.

vein sample G7 (cement generation V) shows an exceptionally large variation in the $\delta^{13}C$ value (relative to their host), but a relative narrow range in $\delta^{18}O$. The variation of $\delta^{18}O$ and $\delta^{13}C$ values in veins with respect to the detected cement generations is shown in Fig. 14c. With exception of the undeformed vein calcite (G7) a weak positive correlation between $\delta^{13}C$ and $\delta^{18}O$ values is observed for all vein-calcites.

6.3. Interpretation

The isotopic ratios of limestone samples of sub-area C and D are within a range of values considered typical for marine carbonates of corresponding age (Veizer & Hoefs, 1976). The $\delta^{18}O$ values of carbonate-bearing host rocks (sandstones) of sub-area A and B are slightly lower than the primary isotopic signature of the Tertiary limestones suggesting an interaction of the host rocks with meteoric fluids or with a marine fluid at elevated temperatures (Verhaert et al., 2004).

Calcite veins with similar isotopic composition as their surrounding host rock have been precipitated from a fluid in which isotopic composition was buffered by the surrounding rock (rock-buffered system, Kenis et al., 2000). This suggests local fluid redistribution between host rock and damage zone. Calcite veins with depleted $\delta^{18}O$ values compared to their host rock indicate fluids ascended or descended from sources at greater distance (depth?). Fluid inclusion data for these veins suggest minimum temperatures between 70 and 170 °C. If we assume such a precipitation temperature range, the oxygen-isotope calcite-water fractionation (ÓNeil et al., 1969) yields $\delta^{18}O$ values of −8 to 8‰ V-SMOW for the fluid from which the vein calcite precipitated. The large variation of $\delta^{18}O$ values can be due to a temperature effect or water-rock interaction or a combination of both (Verhaert et al., 2004). We assume that primary meteoric water was carried upward into the fault and was modified by interaction with rocks at elevated temperatures.

The observed trend of large carbon isotopic fractionation and smaller oxygen fractionation for the undeformed sample G7 is consistent with precipitation of vein-calcite from a near-surface, low-temperature, meteoric fluid in the presence of C^{12}-enriched soil-gas CO_2 (compare Verhaert et al., 2004).

7. Discussion and conclusions

The interdisciplinary approach performed in this study with different types of data along with previous published data (Okay et al., 2004; Motagh et al., 2007) allows us to evaluate the complex fault evolution of the GF over different time scales. The primary purposes of this study are (1) to compare microseismic data with paleostress data, (2) to evaluate the fault structures to better understand fault models, (3) to estimate the role of fluids and fluid-rock interactions in faulting deformation, and (4) to asses faulting conditions of the GF. The conceptual sketch in Fig. 15 summarizes the above-presented fault data and observations.

Recordings from a temporary seismic network at the eastern part of the GF show two clusters of seismic activity with magnitudes below 2.5. The more prominent cluster of activity is located offshore to the North of Marmara Island, which was known to be active also for larger ($M > 2.5$) magnitudes from recordings of the permanent Turkish network. A second cluster with magnitudes $M < 2.5$ is located along the GF trace and below the Ganos mountains. The substantial level of low-magnitude seismicity recorded by our local network suggests that the part of the GF monitored by our network is not fully locked as has been recently suggested by Motagh et al. (2007) but instead is partly creeping. The cumulative fault plane solutions for each seismicity cluster indicate dominantly strike-slip with a minor dip-slip component. The P-axes orientations of the fault plane solutions are in reasonable agreement with the summarized orientation of the paleostress field at the GF (Table 3), which reveals a strike-slip faulting regime with sub-horizontal NW–SE trending orientation of the maximum principle stress. The angle between the σ_1 orientation and the strike of the GF is $<45°$ suggesting that the fault is not anomalously weak (Rutter et al., 2001). At local (sub-area) scale, the maximum principal stress σ_1 varies between NW–SE and E–W.

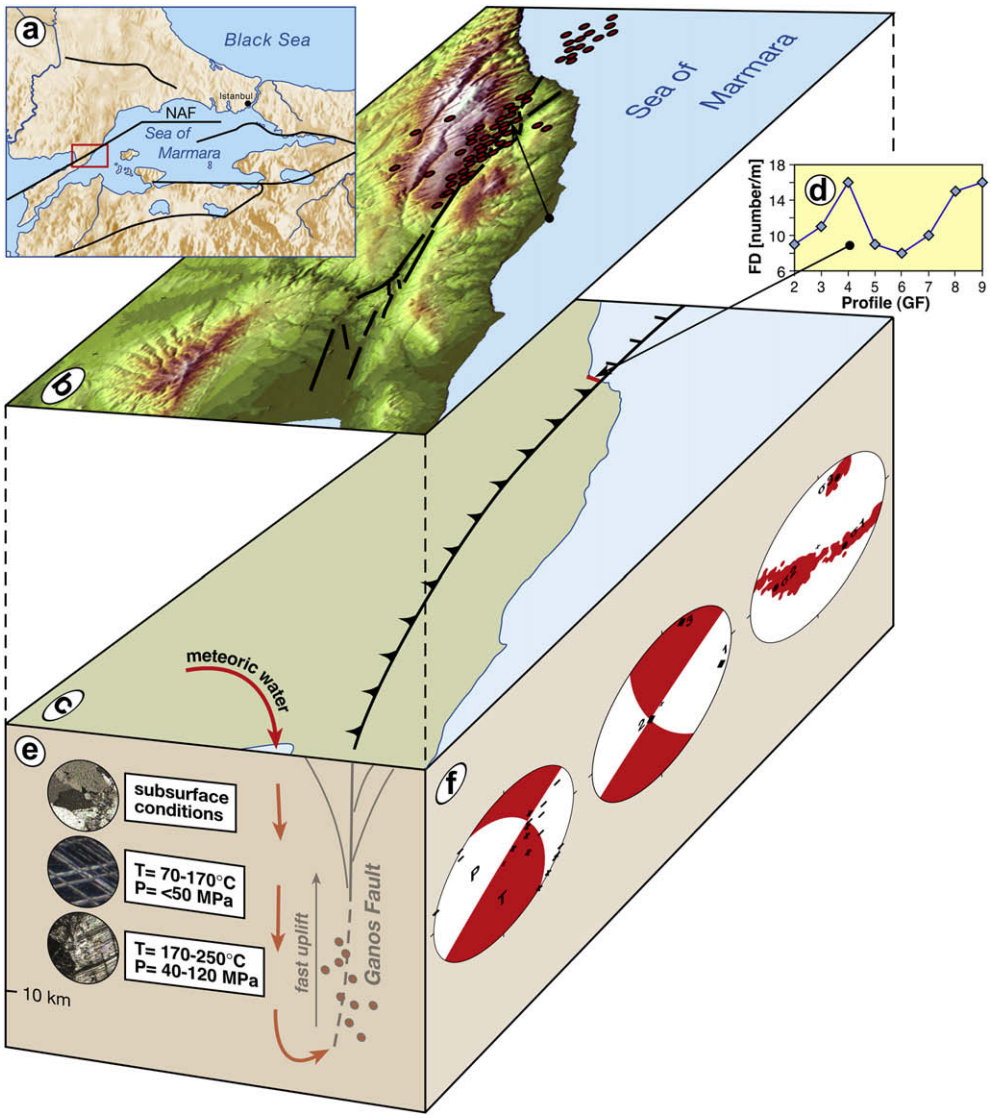

Fig. 15. Conceptual sketch of the Ganos Fault summarizing our results. (a) Regional overview with the North Anatolian Fault. (b) Satellite image of the Ganos fault with the distribution of microseismic events (red circles) registered by our local network. (c) Masked surface illustrating the fault trace with the transition from transpressional to transtensional faulting and the infiltration of meteoric water. (d) Results of structural analysis (number of fractures, subsidiary faults and veins per meter) along a profile normal to the fault. (e) Schematic cross section illustrating uplift and the splaying of the main fault. The sector of circles shows different stages of cementations connected with the derived deformation conditions. The red circles represent the microseismic events. (f) Kinematic analysis and the stress-tensor inversion for the entire database.

The local paleostress field orientation along the GF is almost identical with the long-term regional stress field in NW Turkey derived from the World stress map (Heidbach et al., 2008). Also stress-tensor inversion results of the 11 largest earthquakes that had occurred in the region since 1943 indicate a strike-slip faulting regime with subhorizontal NW–SE trending orientation of the maximum principle stress (Kiratzi, 2002). However, subsidiary faults and fold axes in the vicinity of the GF suggest transpression (Hancock and Erkal, 1990; Tüysüz et al., 1998) in agreement with the fault plane solution of the 1985 Mürefte earthquake ($M = 4.4$; Kalafat, 1995; Table 3). The spatial coexistence of pure strike-slip and transpression suggest spatial and temporal slip partitioning

Table 3
Faulting regime and strain/stress orientation derived from fault structures and fault plain solutions.

Characteristics	Time	Faulting regime	Strain/stress orientation	Authors
Conjugate normal faults	Quaternary-recent	Transpressional	NE–SW extension	Hancock and Erkal (1990)
Meso-structures (faults, joints)	Pliocene- Quaternary	Transpressional	NE–SW extension	Tüysüz et al. (1998)
Fold axes, parallel to the fault	Pliocene- Quaternary	Transpressional	NW–SE shortening	Okay et al. (2004)
Mürefte-Sarköy earthquake	1912	Right-lateral strike –slip with a normal component		Ambraseys and Finkel (1987)
Saros earthquake	1975	Right-lateral strike –slip with a normal component		McKenzie (1978)
Mürefte earthquake	1985	Reverse fault mechanisms		Kalafat (1995)
Secondary faults, striations	Pliocene- Quaternary	Dominant strike-slip regime	NW–SE orientation of σ_1	Here
Microseismic activities	Present	Strike-slip regime with a minor dip component	NW–SE orientation of P-axis	Here

along the GF during its evolution since the latest Miocene until today. Local rotations of the present stress field after the 1999 Izmit earthquake ($M = 7.4$) were also described for the Izmit segment of the NAFZ (Bohnhoff et al., 2006).

Previous conceptual models for the structure of large-displacement faults described two end-member structures of fault zones. The Punchbowl fault (California; USA), which comprises a single fault core centrally located in the damage zone (Chester and Logan, 1986), represents one end-member. The other end-member consists of multiple, anastamosing gouge layers isolating lenses of fractured rocks within a broad damage zone, as in the Carboneras fault (Spain) described by Faulkner et al. (2003).

The GF represents an exhumed fault system characterized by a broad damage zone containing numerous subsidiary faults, rather than a single continuous main fault. These subsidiary faults reveal a transition from fractured rocks to cataclasites and clay gouges. A main fault core with a gouge zone is not exposed. A similar fault structure has been documented along the Dead Sea Transform (DST) where a broad damage zone contains several subsidiary faults with associated small gouge layers (Janssen et al., 2004). In addition, preliminary results from the San Andreas Fault (SAF) Observatory at Depth (SAFOD) define the San Andreas Fault to be relatively broad (~250 m), containing several discrete, highly localized shear zones (Hickman et al., 2007).

A plethora of studies suggest that fluid-rock interactions are strongly linked to a variety of faulting processes. For example, the cyclic nature of earthquake faulting processes results in the repeated change between creation and destruction of permeability due to brittle fracturing and fault healing (Blanpied et al., 1992; Byerlee, 1993; Janssen et al., 2007b). Fluid-assisted fault healing along the GF is restricted to fracture cementation in limestone and turbidite sequences. Fluids penetrating the fault zone, probably originated from two sources. Fluid inclusion and stable isotope data from several generations of calcite veins show that the fluids are predominantly of meteoric origin and migrated upward into the fault. We suggest that the fault taps a warm meteoric fluid reservoir. This would explain the high temperature observed. The calcite cement generations document a change in precipitation conditions (redox potential, temperatures) of this fluid. Pure CH_4 inclusions found in quartz cement suggest biogenic or thermogenic methane. The depth of the source sediments generating the methane is unknown. Our results are in part inconsistent with geochemical investigations of fault rocks from the DST, SAF and the Nojimi Fault (NF). In all these fault systems, fluids are also predominantly of meteoric origin but they migrated downwards at shallow to moderate depth (Lin et al., 2001; Pili et al., 2002; Janssen et al., 2007b). Furthermore, infiltration of seawater and/or brines into the fault as observed at the DST, SAF and NF could not be established for the GF.

We resolved differences in faulting conditions of the GF using two independent techniques: calcite microstructural geothermometry and fluid inclusion analysis. Deformation conditions derived from fluid inclusion data in vein quartz (generation II) reached a maximum temperature of 250 °C and maximum pressures of 120 MPa. For vein-calcite (generation III and IV) fluid inclusion data indicate lower deformation temperatures and pressures (70°–170 °C; <50 MPa). These deformation conditions overlap with those that we obtain from the calcite microstructures (Table 1). Vein-calcite of generation V and quartz veins (generation VI) are completely undeformed. The change in deformation conditions may be explained either by different faulting conditions along a fault or by a temporal variation of deformation intensity. Along the GF no systematic spatial variations of deformation conditions are evident. Instead, crosscutting relationships of veins, fluid inclusion data, and microstructures indicate a temporal change of faulting conditions during permanent uplift.

Acknowledgements

We thank the colleagues from the Kandilli Institute, Istanbul/Turkey and especially Dean Childs und Dogan Aksar for logistical assistance and fruitful discussions. We also thank A, Hendrich for help with drafting. Careful reviews provided by P. Muchez and one anonymous referee are acknowledged.

References

Allmendinger, R.W., 2001. FaultKin 4.0 X. Computer Program with Documentation. Cornell University, Ithaca, NY, USA.
Altunel, E., Meghraoui, M., Akyüz, S.H., Dikbas, A., 2004. Characteristics of the 1912 co-seismic rupture along the North Anatolian Fault zone (Turkey): implications for the expected Marmara earthquake. Terra Nova 16, 198–204.
Ambraseys, N.N., 1970. Some characteristics features of the North Anatolian Fault Zone. Tectonophysics 9, 143–165.
Ambraseys, N.N., 2001. Reassessment of earthquakes, 1900–1999, in the Eastern Mediterranean and the Middle East. Geophysical Journal International 145, 471–485.
Ambraseys, N.N., Finkel, C.F., 1987. The Saros-Marmara Earthquake of the 9 August 1912. Earthquake Engineering and Structural Dynamics 15, 189–211.
Armijo, R., Meyer, B., Hubert, A., Barka, A., 1999. Westward propagation of the North Anatolian fault into the northern Aegean: timing and kinematics. Geology 27, 267–270.
Armijo, R., Pondard, N., Meyer, B., Mercier de Lepinay, B., Ucarkus, G., Malavieille, J., Dominguez, S., Gustcher, M.-A., Beck, Çagatay, N., Cakir, Z., Imren, C., Kadir, E., Natalin, Marmarascarps Cruise party, 2005. Submarine fault scarps in the Sea of Marmara pull-apart (North Anatolian Fault): implications for seismic hazard in Istanbul. Geochemistry Geophysics Geosystems 6, doi:10.1029/2004GC000896.
Bakker, R.J., 2003. Package *FLUIDS* 1. Computer programs for analysis of fluid inclusion data and for modeling bulk fluid properties. Chemical Geology 194, 3–23.
Barka, A.A., 1992. The North Anatolian fault zone. Annales Tectonicae 6, 164–195.
Barka, A.A., Kadinsky-Cade, K., 1988. Strike-slip fault geometry in turkey and its influence on earthquake activity. Tectonics 7, 663–684.
Barka, A.A., Akyüz, H., Altunel, E., Sunal, G., Çakir, Z., Dikbas, A., Yerli, B., Armijo, R., Meyer, B., Chabalier, J., 2002. The surface rupture and slip distribution of the 17 august 1999 Izmit earthquake (M 7.4), North Anatolian Fault. Bulletin of the Seismological Society of America 92 (1), 43–60.
Baumbach, M., Bindi, D., Grosser, H., Milkereit, C., Parolai, S., Wang, R., Karakisa, S., Zünbül, S., Zschau, J., 2003. Calibration of an M1 Scale in Northwestern Turkey from 1999 Izmit aftershocks. Bulletin of the Seismological Society of America 93 (5), 2289–2295.
Bindi, D., Parolai, S., Gorgun, E., Grosser, H., Milkereit, C., Bohnhoff, M., Durukal, E., 2007. M l scale in northwestern Turkey from 1999 Izmit aftershocks; updates. Bulletin of the Seismological Society of America 97 (1), 331–338.
Blanpied, M.L., Lockner, D.A., Byerlee, J.D., 1992. An earthquake mechanism based on rapid sealing of faults. Nature 358, 574–576.
Bodnar, R.J., Vityk, M.O., 1994. Interpretation of microthermometric data for H2O-NaCl fluid inclusions. In: De Vivo, B., Frezzotti, M.L. (Eds.), Short Course of the Working Group (IMA) Fluid Inclusions in Minerals: Methods and Applications. Virginia Tech, Blacksburg, pp. 117–130.
Boğaziçi University Kandilli Observatory and Earthquake Research Institute (KOERI). Available from: http://www.koeri.boun.edu.tr/sismo/veri_bank/mainw.htm.
Bohnhoff, M., Grosser, H., Dresen, G., 2006. Strain partitioning and stress rotation at the North Anatolian fault zone from aftershock focal mechanisms of the 1999 Izmit Mw = 7.4 earthquake. Geophysical Journal International, doi:10.1111/j.1365-246X.2006.03027.
Borisenko, A.S., 1977. Study of the salt composition of solutions in gas–liquid inclusions in minerals by the cryometric method. Soviet Geology and Geophysics 18, 11–19.
Burkhard, M., 1993. Calcite-twins, their geometry, appearance and significance as stress-strain markers and indicators of tectonic regime: a review. Journal of Structural Geology 15, 351–368.
Byerlee, J., 1993. Model for episode flow of high-pressure water in fault zones before earthquake. Geology 21, 303–306.
Chester, F.M., Logan, J.M., 1986. Implication for mechanical properties of brittle faults from observations of Punchbowl fault zone, California. Pure and Applied Geophysics 124, 79–106.
Duan, Z., Møller, N., Weare, J.H., 1996. A general equation of state for supercritical fluid mixtures and molecular dynamics simulation of mixture *PVTX* properties. Geochimica et Cosmochimica Acta 60, 1209–1216.
Faulkner, D.R., Lewis, A.C., Rutter, E.H., 2003. On the internal structure and mechanics of large strike-slip fault zones: field observations of the Carboneras fault in southern Spain. Tectonophysics 367, 235–252.
Ferrill, D.A., 1998. Critical re-evaluation of differential stress estimates from calcite twins in coarse-grained limestone. Tectonophysics 285, 77–86.

Ferrill, D.A., Morris, A.P., Evans, M.A., Burkhard, M., Groshong, R.H., Onasch, C.M., 2004. Calcite twin morphology: a low-temperature deformation geothermometer. Journal of Structural Geology 26, 1521–1529.

Götze, J., Plötze, M., Habermann, D., 2001. Origin, spectral characteristics and practical applications of the cathodoluminescence (CL) of quartz – a review. Mineralogy and Petrology 71, 225–250.

Hancock, L., Erkal, T., 1990. Enigmatic normal faults within the European sector of the North Anatolian transform fault zone. Annales Tectonicae IV (Special Issue), 171–181.

Heidbach, O., Fuchs, K., Müller, B., Reinecker, J., Sperner, B., Tingay, M., Wenzel, F., 2008. The World stress map – release 2008. Available from: www.world-stress-map.org.

Hickman, S., Zoback, M., Ellsworth, W., Kirschner, D., Solum, J., 2007. Structure and composition of the San Andreas fault at seismogenic depth: recent results from the SAFOD experiment. EOS Trans AGU 88(52), Fall Meeting Supplement, abstract T44B-01.

Hubert-Ferrari, A., Barka, A., Jacques, E., Nalbant, S., Meyer, B., Armijo, R., Tapponnier, P., Geoffrey, C.P., 2000. Seismic hazard in the Marmara sea region following the 17 August 1999 Izmit earthquake. Nature 404, 269–273.

Hudson, J.A., Priest, S.D., 1983. Discontinuity frequency of rock masses. International Journal of Rock Mechanics and Mining Sciences 20, 73–89.

Jamison, W.R., Spang, J.H., 1976. Use of calcite twin lamellae to infer differential stress. Geological Society of America Bulletin 87, 868–872.

Janssen, C., Laube, N., Bau, M., Gray, D.R., 1998. Fluid regime in faulting deformation of the Waratah Fault Zone, Australia, as inferred from major and minor element analyses and stable isotopic signatures. Tectonophysics 294, 109–130.

Janssen, C., Romer, R.L., Hoffmann-Rothe, A., Kesten, D., Al-Zubi, H., 2004. The Dead Sea Transform: evidence for a strong fault. Journal of Geology 112, 561–575.

Janssen, C., Hoffmann-Rothe, A., Bohnhoff, M., Wetzel, H.U., Matar, A., Khatib, M., 2007a. Different styles of faulting deformation along the Dead Sea Transform and possible consequences for the recurrence of major earthquakes. Journal of Geodynamic 44, 66–89.

Janssen, C., Romer, R.L., Plessen, B., Naumann, R., Hoffmann-Rothe, A., Matar, the DESERT Research Group, 2007b. Contrasting fluid regime along the Dead Sea Transform. Geofluids 7, doi:10.1111/j.1468-8123.2007.00185.

Kalafat, D., 1995. Study of the tectonic structures in Anatolian based on fault mechanism solutions. PhD thesis, University of Istanbul, 217 pp. (in Turkish).

Karabulut, H., Bouin, M.P., Bouchon, M., Dietrich, M., Cornou, C., Aktar, M., 2002. The seismicity in the Eastern Marmara Sea after the 17 August 1999 Izmit Earthquake. Bulletin of the Seismological Society of America 92, 387–393.

Kenis, I., Muchez, P.H., Sintubin, M., Mansy, J.L., Lacquement, F., 2000. The use of a combined structural, stable isotope and fluid inclusion study to constrain the kinematic history at northern Variscan front zone (Bettrechnies, northern France). Journal of Structural Geology 22, 589–602.

Kiratzi, A., 2002. Stress tensor inversions along the westernmost North Anatolian fault zone and continuation into the northern Aegean Sea. Geophysical Journal International 151, 360–376.

Lienert, B.R., Havskov, J., 1995. HYPOCENTER 3.2 a computer program for locating earthquakes locally, regionally and globally. Seismological Research Letters 66, 26–36.

Lin, A., Tanaka, N., Uda, S., Satish-Kumar, M., 2001. Infiltration of Meteoric and Sea water into deep fault zones during episodes of coseismic events: a case study of the Nojima Fault, Japan. Bulletin of the Earthquake Research Institute, University of Tokio 76, 341–353.

McKenzie, D.P., 1978. Active tectonics of the Alpine-Himalayan Belt. The Aegean Sea and surrounding regions. Geophysical Journal of the Royal Astronomical Society 55, 217–254.

Maret, R., Allmendinger, R.W., 1990. Kinematic analysis of fault-slip data. Journal of Structural Geology 12, 973–986.

Meyers, W.J., 1974. Carbonate cement stratigraphy of the Lake Valley Formation Mississippian, Sacramento Mountains, New Mexico. Journal of Sedimentary Petrology 44, 837–861.

Meyers, W.J., 1978. Carbonate cements: their regional distribution and interpretation in Mississippian limestones of southwestern New Mexico. Sedimentology 25, 371–400.

Michael, A.J., 1991. Spatial variations in stress within the 1987 Whittier Narrows, California, aftershock sequence. New techniques and results. Journal of Geophysical Research 96, 6303–6319.

Motagh, M., Hoffmann, J., Kampes, B., Baes, M., Zschau, J., 2007. Strain accumulation across the Gazikoy-saros segment of the North Anatolian Fault inferred from persistent scatterer interferometry and GPS measurements. Earth and Planetary Science Letters 255, 432–444.

Okay, A., Demirbag, E., Kurt, H., Okay, N., Kuscu, I., 1999. An active, deep marine strike-slip basin along the North Anatolian Fault in Turkey. Tectonics 18, 129–147.

Okay, A., Tüysüz, O., Kaya, S., 2004. From transpression to transtension: changes in morphology and structure around a bend on the North Anatolian Fault in the Marmara region. Tectonophysics 391, 259–282.

ÓNeil, J.R., Clayton, R.N., Mayeda, T.K., 1969. Oxygen isotope fractionation in divalent metal carbonates. Journal of Chemical Physics 51, 5547–5558.

Pili, E., Poitrasson, F., Gratier, J.P., 2002. Carbon-oxygen isotope and trace element constraint on how fluids percolate faulted limestones from the San Andreas Fault system: partitioning of fluid sources and pathways. Chemical Geology 190, 231–250.

Reilinger, R., McClusky, S., Vernant, P., Lawrence, S., Ergintav, S., Cakmak, R., Ozener, H., Kadirov, F., Guliev, I., Stepanyan, R., Nadariya, M., Hahubia, G., Mahmoud, S., Sakr, K., Guseva, T., Evren, E., Dmitrotsa, A., Filikov, S.V., Gomez, F., Al-Ghazzi, R., Karam, G., 2006. GPS constraints on continental deformation in the Africa-Arabia-Eurasia continental collision zone and implications for the dynamics of plate interactions. Journal of Geophysical Research 111 (B5), doi:10.1029/2005JB004051.

Rowe, K.J., Rutter, E.H., 1990. Paleostress estimation using calcite twinning: experimental calibration and application to nature. Journal of Structural Geology 12, 1–17.

Rutter, E.H., Holdsworth, R.E., Knipe, R.J., 2001. The nature and tectonic significance of fault zone weakening: an introduction. In: Holdsworth, R.E., Strachan, R.A., Magloughlin, J.F., Knipe, R.J. (Eds.), The Nature and Tectonic Significance of Fault Zone Weakening. Geological Society (London) Special Publication, vol. 186, pp. 1–11.

Schulz, S.E., Evans, J.P., 2000. Mesoscopic structure of the punchbowl fault, southern California and the geological and geophysical structure of active strike-slip fault. Journal of Structural Geology 22, 913–930.

Seeber, L., Emre, O., Cormier, M., Sorlien, C., McHugh, C., Polonia, A., Ozer, N., Cagatay, N., 2004. Uplift and subsidence from oblique slip: the Ganos-Marmara bend of the North Anatolian Transform, Western Turkey. Tectonophysics 391, 239–258.

Sengör, A.M.C., 1979. The North Anatolian transform fault: its age, offset and tectonic significance. Journal of the Geological Society (London) 136, 269–282.

Sengör, A.M.C., Tüysüz, O., Imren, C., Sakinc, M., Eyidogan, H., Görür, N., Pichon, X., Rangin, C., 2005. The North Anatolian Fault: a new look. Annual Review of Earth and Planetary Sciences 33, 37–112.

Sentürk, K., Sümengen, M., Terlemez, I., Karaköse, C., 1998. Bandirma D-4 Sheet and 10 Page Explanatory Text, 1:100 000 Scale, Geological Map Series. General Directorate of Mineral Research and Exploration, Ankara.

Snoke, J.A., 2003. FOCMEC: focal mechanism determinations. In: Lee, W.H.K., Kanamori, H., Jennings, P.C., Kisslinger, C. (Eds.), International Handbook of Earthquake and Engineering Seismology. Academic Press, San Diego Chapter 85.12.

Tibi, R., Bock, G., Xia, Y., Baumbach, M., Grosser, H., Milkereit, C., Karakisa, S., Zünbül, S., Kind, R., Zschau, J., 2001. Rupture processes of the 1999 August 17 Izmit and November 12 Düzce (Turkey) earthquakes. Geophysical Journal International 144, F1–F7.

Tüysüz, O., Barka, A., Yigitbas, E., 1998. Geology of the Saros graben and its implications for the evolution of the North Anatolian fault in the Ganos-Saros region. Tectonophysics 293, 105–126.

Veizer, J., Hoefs, J., 1976. The nature of $\delta^{18}O/\delta^{16}O$ and $\delta^{13}C/\delta^{12}C$ secular trends in carbonate rocks. Geochimica et Cosmochimica Acta 40, 1387–1395.

Verhaert, G., Muchez, P., Sintubin, M., Similox-Tohon, D., Vandycke, S., Keppens, E., Hodge, E.J., Richards, D.A., 2004. Origin of palaeofluids in a normal fault setting in the Aegean region. Geofluids 4, 300–314.

Yaltirak, C., Alpar, B., Sakinc, M., Yüce, H., 2000. Origin of the Strait of Canakkale (Dardanelles): regional tectonics and the Mediterranean-Marmara incursion. Marine Geology 164, 139–156.

Yaltirak, C., 2002. Tectonic evolution of the Marmara Sea and its surroundings. Marine Geology 190, 493–529.

Yaltirak, C., Alpar, B., 2002. Kinematics and evolution of the northern branch of the North Anatolian Fault (Ganos Fault) betweeen the Sea of Marmara and the Gulf of Saros. Marine Geology 190, 351–366.

Zattin, M., Okay, A., Cavazza, W., 2005. Fission-Track evidence for late Oligocene and mid-Miocene activity along the North Anatolian Fault in south-western Trace. Terra Nova 17, 95–101.